Title
Dynamics and Interactions of Organic Molecules Bound to the Cu(111) Surface

Author
Wyrick, Jonathan Eugene

Publication Date
2013

UNIVERSITY OF CALIFORNIA
RIVERSIDE

Dynamics and Interactions of Organic Molecules Bound to the Cu(111) Surface

A Dissertation submitted in partial satisfaction
of the requirements for the degree of

Doctor of Philosophy

in

Physics

by

Jonathan Eugene Wyrick

December 2013

Dissertation Committee:
Dr. Ludwig Bartels, Chairperson
Dr. Theodore L. Einstein
Dr. Vivek Aji

The Dissertation of Jonathan Eugene Wyrick is approved:

Committee Chairperson

University of California, Riverside

ACKNOWLEDGEMENTS

First and foremost I would like to thank my adviser, Ludwig Bartels whose unique management style I have found to be most helpful in my own development and research successes. He appears to have two complimentary approaches that help students be productive and graduate in a timely fashion (typically within 4 or 5 years, which is really quite impressive in the experimental realm). Firstly, Ludwig is a fierce advocate for his students and will put whatever resources he has to bear on aiding us in our time(s) of need: for example, when my co-worker Yeming was unable to return to the US from Mexico, it was Ludwig who made Yeming's return possible, and when I unknowingly attempted to subvert UCR's Condensed Matter Physics course requirements Ludwig handled the surprisingly (to me) large fallout without requiring any involvement on my part. Ludwig's second management technique that I experienced was to flood me with projects, keeping me very much on my toes, and I have many results to show for it. At the heart of it, Ludwig genuinely cares about helping the students he interacts with make significant accomplishments and grow in our field of research. I also saw this same attitude towards undergraduates outside of his lab as his TA (a very time-consuming and demanding job by the way) as he employed a dizzying variety of techniques (all thought up and developed by him I believe) for maximally engaging students and immersing them in the subject at hand; I feel that he tries to put that same kind of time and (dizzying) attention into the growth of each of the students in his lab. I wish Ludwig all the luck in the world in figuring out how to continue these kinds of efforts as our lab size has more than doubled in the last year (both in number of students as well as physical space).

I also owe a great deal to the experimentalists in our lab (see individual contributions below), particularly Yeming with whom I worked quite closely on the project described in

Chapter 3. While the content of the papers contained herein consists mostly of the analyses and theoretical work that I performed, the underlying experiments presented in each represent a much greater number of man/woman-hours on the collective parts of the experimentalists who contributed – without their work, there would be nothing (in which case this dissertation would be much shorter, so perhaps some blame can be shared by them as well). Each paper really represents a collaboration between most or all of the members of our group (at the time of writing) even if the physical space taken up in each is mostly dedicated to analysis, discussion, and other forms of attempting to make theoretical sense of the experimental data.

During my time at UCR I had several opportunities to meet with collaborators on the east coast. Ted Einstein and his postdoc Kwangmoo Kim at UMD were always very helpful when I visited, and a lot of interesting research came out of our interactions. As can be seen below, Ted has been very influential in all of my efforts. Having worked quite closely with Ted I've enjoyed his own personal brand of humor, as well as his unique office organization scheme: I hope that when I have an office of my own I can successfully reproduce the filing system he has implemented.

Also on the East coast, at UCF, is our collaborator Talat Rahman. When I visited I always felt most welcome, as Talat provides wonderful hospitality, especially in the form of really excellent, home-cooked Pakistani food. Beyond that, Talat is a first rate computational theorist, and she and her group always expended great effort to train me (and fellow co-workers) in the meaning of, and proper way to perform Density Functional Theory (DFT) calculations. Duy Le, and Sampyo Hong of her group provided us with well thought-out tutorials on the subject and I appreciate the time they spent putting their ideas and materials together in a coherent fashion. Duy in particular has acted as a mentor to me with regards to DFT so I owe him many thanks for all of his help and advice. I also found all of the other members of Talat's group to be welcoming and enjoyed working with them whenever I visited.

I have also found great support in some of our overseas collaborators, Per Hyldgaard and Kristian Berland. Though I only met Per once, at a conference, he and Kristian were able to collaborate quite effectively with us via internet. Their contributions in terms of knowledge and ideas, as well as their calculation contributions were most helpful in my work (see below) – the theoretical underpinnings of surface state substrate mediated interactions between adsorbates is due to Per and Ted's works on the matter. Also I believe Kristian has cited the paper we collaborated on in several of his works, so I should thank him for upping my citation count as well!

Though I spent most of my time researching on the opposite side of the country from my family, they have supported me from a distance and I appreciate that support very much. My father also performed my wedding ceremony to my wife Satoko during my time at UCR; so I am very indebted to him for that, as well as to my mother, my sister and brother, and Satoko's father, mother, and sister who flew here from Japan to attend the ceremony.

I would also like to acknowledge my co-worker John Mann, whose projects did not overlap with mine, but was always willing and interested to discuss my work as well as letting me eavesdrop on his projects. We started gradschool the same year, in the same department (Physics) – he switched to Materials Science half way through, yet as a result of an amazing whirlwind of productivity has managed to finish at the same time as me (on the same day no less). Throughout it all he has been an excellent friend and has provided much needed support through the ups and downs (many of these) of gradschool.

Finally I would like to thank Mark, Chen, and Jessica for being great students (having done quite well in learning DFT calculations from me). I wish them the best of luck in continuing the tradition of imbedded theorists in the Bartels lab.

The text of this dissertation, Chapters 3 through 6 respectively, is a reprint of the material as it appears in:

Journal of Physics: Condensed Matter 2012 [3]

My contributions: I wrote the text of this paper in direct collaboration with PI Ludwig Bartels. All analyses and development of theoretical models were performed either by me directly, or under my guidance. I also assisted with the experimental investigations.

Co-authors contributed as follows: Yeming Zhu headed the experimental effort and was assisted by KatieMarie Magnone (an excellent lab safety manager by the way). Kamelia D Cohen, Connor Holzke, and Daniel Salib performed some of the DFT calculations. Quan Ma and Dezheng Sun contributed to the experimental effort as well. Ludwig Bartels contributed much input in the development of the theoretical models.

Nano Letters 2011 [4]

My contributions: I wrote the text of this paper in direct collaboration with PI Ludwig Bartels and collaborator Ted Einstein. I developed the model that is the central topic of this paper, and performed the necessary coding and analyses to test it.

Co-authors contributed as follows: Daeho Kim, Dezheng Sun, Zhihai Cheng, Wenhao Lu, Yeming Zhu, Eli Rotenberg, and Miaomiao Luo contributed the experimental data upon which the theoretical model was based. Kristian Berland and Per Hyldgaard provided calculations determining the band bottom shift of the surface state due to adsorption of the molecules studied on Cu (111). Ted Einstein provided several key insights, the fact that my results could be viewed as describing quantum dots in particular. As above, Ludwig Bartels contributed much input in the development of the theoretical models.

Physical Review Letters 2010 [5]

My contributions: I wrote the text of this paper in direct collaboration with PI Ludwig Bartels and collaborator Ted Einstein. As in the previous paper, I developed the model that is the central topic of this paper, and performed the necessary coding and analyses to test it. I also assisted in the preliminary analysis (tracking of the movements of CO) of the raw data.

Co-authors contributed as follows: Postdoc Zhihai Cheng headed the experimental effort and was aided by Miaomiao Luo, Dezheng Sun, Dahoe Kim, Yeming Zhu, and Wenhao Lu, all of whom also assisted in tracking the movements of CO in the acquired raw image data. Kwangmoo Kim and Ted Einstein supplied Monte-Carlo results related to the system studied, and contributed useful discussions and advice regarding the substrate mediated interactions associated with the Cu (111) surface state. And of course, Ludwig Bartels contributed much input in the development of the theoretical models.

Nano Letters 2010 [6]

My contributions: I wrote the text of this paper in direct collaboration with PI Ludwig Bartels and collaborator Ted Einstein. I performed the statistical and energetic analyses presented in this paper.

Co-authors contributed as follows: The system studied in this paper is the same as the PRL paper mentioned above, however the analysis in this case focuses on the statistical behavior observed – therefore many of the contributions from co-authors are the same as above. Zhihai Cheng, Miaomiao Luo, Dezheng Sun, Daeho Kim, Yeming Zhu, and Wenhao Lu contributed the experimental data. Kwangmoo Kim and Ted Einstein supplied Monte-Carlo results related to the system studied, and contributed useful discussions and advice regarding the Statistical Mechanics involved. Ludwig Bartels contributed much input on the interpretation of the statistical analysis.

The text of Chapter 7 is a manuscript that we currently intend to publish in:

Journal of Chemical Physics

My contributions: I wrote the text of this paper in direct collaboration with PI Ludwig Bartels. I developed the technique presented and applied it to previous experimental results from our lab.

Co-authors contributed as follows: Ludwig Bartels contributed the initial idea that there should be some way to understand our experimental data in terms of a molecular orbital theory picture.

I gratefully acknowledge support by DOE (DE-FG02-07ER15842), AFOSR (FA9550-08-1-0401), joint NSF (CHE 07-49949 and CHE 07-50334 under Ludwig Bartels and Ted Einstein respectively), and the Swedish Research Council (621-2008-4346 under Per Hyldgaard). This research used resources of the National Energy Research Scientific Computing Center (NERSC), which is supported by DOE (DE-AC02-05CH11231).

DEDICATION

I dedicate this dissertation to my wife Satoko and our dog Al Einstein for their unending love and support. In particular I thank Satoko for keeping me mostly sane, and Al for his many insistences that I not take the probabilistic underpinnings of Quantum Mechanics on good faith (though based on the empirical data so far, Quantum Mechanics appears to be well founded).

ABSTRACT OF THE DISSERTATION

Dynamics and Interactions of Organic Molecules Bound to the Cu(111) Surface

by

Jonathan Eugene Wyrick

Doctor of Philosophy, Graduate Program in Physics
University of California, Riverside, December 2013
Dr. Ludwig Bartels, Chairperson

The progress of modern technology is dominated by shrinking component size (with a goal of reaching angstrom scale resolution), particularly with respect to electronics and optimization of common industrial processes such as heterogeneous catalysis. Understanding of such systems lies at the upper end of applicability for first-principles calculations and existing theoretical models, and a scientific framework is needed to understand, predict, and control these systems at the molecular level. My research has focused on organic molecules adsorbed on a Cu(111) surface as model systems, studied experimentally by means of scanning tunneling microscopy (STM) as well as theoretically by density functional theory (DFT) and development of simplified explanatory models. Results of this investigation show that: 1) on Cu (111) full mono-layer coverages of acetylene undergo long-range ordering which at short-range is driven by a need to minimize localized stress induced in the upper substrate layers by adsorption while at longer ranges DFT finds an oscillatory interaction that correlates well with the surface state, 2) long-range ordered networks of anthraquinone (AQ) are found to mold the surface state into

optimized quantum dots – this need for optimization under the constraint that neighbors must form H-bonds drives formation of the network at the precise size and shape observed in STM, 3) CO molecules co-adsorbed into the AQ network's pores titrate the surface state quantum dots and experience increased mobility, 4) the adsorption of anthracene modified with chalcogen linkers onto Cu (111) when viewed within a molecular orbital theory framework yields a chemical explanation for the diffusion behavior observed in STM. In combination, these observations and derived explanatory models help to characterize and quantify the fundamental physics underlying the interactions of adsorbates with one another and with the Cu (111) substrate, in a broader context acting as a model for other confined surface systems where the same kinds of interactions play a dominant role.

TABLE OF CONTENTS

TABLE OF FIGURES

Chapter 1 Introduction

1.1 Overview

This dissertation is a compilation of the work I have done as a member of the Bartels research group, an experimental group in the area of Physical Chemistry. My work, however, has been primarily theoretical in nature, complementing and providing insight into the scanning tunneling microscopy (STM) studies that have been performed in our lab. The underlying theme that ties each of the studies presented here together is that they are all attempts to observe and make sense of the fundamental physics and chemistry involved in the behavior of organic molecules adsorbed to a Cu (111) surface.

The analyses I have performed on these types of systems fall into two broad categories: 1) calculations to directly interpret acquired STM data and 2) formulation of physical models to explain the behavior observed in the STM data. In the first case ab-initio electronic structure calculations are performed using Density Functional Theory (DFT) while in the second case, calculations and model development are performed at whatever degree of simplification is appropriate given the nature of the problem and the data available. In this introductory chapter I will therefore provide a brief introduction to DFT (section 1.2) as well as discuss the software and computational resources used to perform DFT calculations (section 1.3). Chapter 2 provides an introduction to STM from a theoretical perspective and details how low temperature STM images can be interpreted by comparing to electronic structure calculations – these techniques are then put to use in Chapter 3 where the details of adsorption of a monolayer of acetylene to the Cu (111) surface are deduced from STM images. Chapters 4 through 6 are concerned with using simplified models to understand the formation of long-range ordered networks of anthraquinone (AQ) on Cu (111) and then using those networks as a system of regular pores to study the effects of 2D confinement that they impose on subsequently deposited CO molecules. Finally, in chapter 7 I develop a molecular orbital theory interpretation of DFT calculations in order to understand the effects of electronic structure on the adsorption and diffusion of three related anthracene derivatives (one of which is AQ, the same molecule studied in chapters 4 through 6) on Cu (111).

1.2 Introduction to DFT

DFT is a method for determining the ground state electronic density of a many-body electronic system. The key insight of DFT is that if a system is in its ground electronic state, then the associated electron density contains all of the knowable information of the many-body electronic system; knowing this density is tantamount to knowing all of a ground-state system's properties. Its use applies to systems in which a zero temperature assumption is appropriate and additionally relies on the Born-Oppenheimer approximation allowing for determination of the minimum energy geometries of molecules and crystals according to the Hellman-Feynman theorem. DFT has enjoyed some measure of success in the past decades due to the fact that compared to other ab-initio techniques of similar accuracy, it is computationally inexpensive. The reason for this is that DFT focuses on electron density $n(\vec{r})$ as its fundamental quantity whereas more traditional techniques focus on the many-electron wave function $\varphi(\vec{r}_1\, \vec{r}_2 \dots \vec{r}_N)$, which can itself most generally be written as a (potentially infinite) linear combination of Slater determinants of single-electron wave functions (i.e. it is a member of Fock-space). So, ignoring spin, a problem with 3N variables (where for systems of interest the number of electrons N is quite large) has been reduced to one with 3 (at least in principle).

The ground state is found by minimizing a functional whose output is the system's electronic ground state energy and whose input is the density. That is, the ground state energy is given by $E_0 = E_0[n]$, and the ground state density n_0 is that density n for which $E_0[n]$ is minimized. That this is at all possible was established in 1964 by Kohn and Hohenberg.[7] Unfortunately, however, their proof was not a constructive proof: they showed that such an energy functional exists but not the details of its mathematical form. A year later in 1965 Kohn and Sham developed a commonly used scheme to approximate the (to-this-date) yet unknown "universal" energy functional.[8] They did this by exchanging the problem of working with the density (n) of a system of interacting electrons for working with the density (n_s) of an auxiliary system of independent electrons under the influence of a potential designed to yield $n_s(\vec{r}) = n(\vec{r})$. Because the auxiliary electrons are independent, the auxiliary density can be written as $n_s(\vec{r}) = \sum_{i=1}^{N} \langle \varepsilon_i | \vec{r} \rangle \langle \vec{r} | \varepsilon_i \rangle$ where the $|\varepsilon_i\rangle$ are called the Kohn-Sham (KS) orbitals; as such, they are considered to be effective orbitals, acting as single-particle wave-vectors representing each of the independent electrons of the fictitious non-interacting system.

Similar reasoning as applies to the well-known Hartree-Fock (HF) method applies here: the Kohn-Sham orbitals can each be considered to be solutions to their own single-particle Schrödinger-like equation (called a KS equation):

$$(\hat{T}_S + \hat{V}_S[n])|\varepsilon_i\rangle = \varepsilon_i |\varepsilon_i\rangle \,,$$

where $\hat{T}_S$ is the standard single-particle kinetic energy operator and $\hat{V}_S[n]$ is a potential operator which itself is a functional of the density n. Since the density depends on the KS orbitals, the above equations must be solved iteratively, where an initial guess for the electron density is supplied, the KS equations are solved using that original density and then their orbitals are used to generate a new "improved" density that is input into the next iteration. The final density n_s

that is found after some number of iterations is said to be self consistent in that, when input into $\hat{V}_S[n]$ in the KS equation, it yields KS states whose calculated total density is n_s (if this were not the case, then the KS equations would not be consistent with themselves).

There are at least two advantages and one disadvantage that I can think of to this technique. The disadvantage is that the 3 variable problem of solving for the density has now been replaced with a 3N variable problem of finding the auxiliary single-particle KS orbitals; this is considered acceptable because at least now the KS orbitals can be solved pseudo-independently from one another (they are not truly independent in so much as the potential is updated each iteration with all of the KS orbitals combined), which is still better than e.g. trying to work with a linear combination of Slater determinants rather than just one.

One advantage of this technique is that it allows us to separate the problem of approximating the universal functional into 1) parts that are well known in terms of either single-particle wave-functions or in terms of the density, and 2) parts that are approximated (because their dependence on the aforementioned variables is not known, or out of convenience; for example, the HF exact exchange energy could be included as a "known" term, however is often approximated instead). The "well known" parts include: the non-interacting kinetic energy, the original potential from the interacting problem (due to the atomic nuclei), and the potential due to interaction of each electron with the mean field of all other electrons in the system. Everything that is left is lumped together and called the exchange-correlation functional, for which there is an annoying abundance of approximations (each potentially useful for certain classes of systems, but none of which that is universally applicable).

The second advantage alluded to above is that the KS orbitals themselves, while not having a precise physical meaning beyond being an auxiliary system of orbitals, do act as a perfectly good basis (they are ortho-normal to one another and form a complete set) with which to decompose the system whose ground state they were used to calculate, or as will be discussed in chapter 7, any closely related system. In this sense they can be thought of as providing "chemical" insight even if their precise physical meaning is not well understood (at the very least, the KS orbitals offer a mathematically well-defined partitioning of the total charge density which does have a precise physical meaning); in fact, it has been argued that the KS orbitals provide an equally good, if not better basis for an molecular orbital theory analysis.[9, 10]

Finally, for those readers who would prefer to see derivations of the fundamental concepts of DFT in rigorous detail, I suggest [11, 12] and/or [13]. These books won't help anyone perform any actual DFT calculations, but provide a solid mathematical and physical foundation as to why DFT calculations can be believed to solve the many-body electronic ground state problem in the first place; in my opinion, it is important to check whether your tools actually function as advertized.

1.3 Software and Resources used for DFT and other Calculations

Despite the comparative efficiency of DFT to other ab-initio methods, it is still computationally costly and in order to investigate systems of interest it is necessary to bring many resources to bear. The software used for the calculations presented herein consisted primarily of Vienna Ab-initio Simulation Package (VASP) and Mathematica.

VASP takes a set of atomic coordinates as well as what specific atoms are located at those coordinates as input, performs DFT calculations on those input systems, and then outputs relevant information about their electronic structure and the final geometries they assume as a result of energy minimization. Because DFT is fundamentally an approximation (particularly in the absence of a “universal” energy functional), and because it is performed on computers which themselves are only capable of manipulating discrete and finite quantities, it is also necessary to specify many additional input parameters aimed at optimizing the quality of the calculations performed while not overburdening the computational resources being utilized. Additionally, the input and output of VASP consist only of text files (and one large binary file whose internal data format/arrangement is poorly documented), and VASP provides little in the way of analysis tools or user interfaces. For these reasons I developed a library of Mathematica functions to aid in generating appropriate input as well as being able to manipulate and analyze the raw output of VASP into useful information. Mathematica notebooks also provide a nice analog to the concept of a lab notebook in that one can keep a somewhat chronological record of calculations performed on any given problem (if one chooses to).

The modeling and calculations that I performed in chapters 4 through 6 do not include DFT calculations (except by collaborators) but instead involve statistical tracking of diffusing molecules as well as single-particle type calculations to create models of the systems concerned. These works were also performed using Mathematica notebooks.

As already noted, VASP calculations require substantive computational resources in order to produce useful data during the limited lifespan of a human being. For this reason I assembled a small linux cluster of computers purchased from various sources with the dedicated purpose of performing VASP calculations. I also wrote software (in Java) to allow monitoring of calculations in progress from a web page (figure 1.1). Additionally we have limited access to resources at the National Energy Research Scientific Computing Center (NERSC) which were also used for many of the VASP calculations reported on in this collection of works.

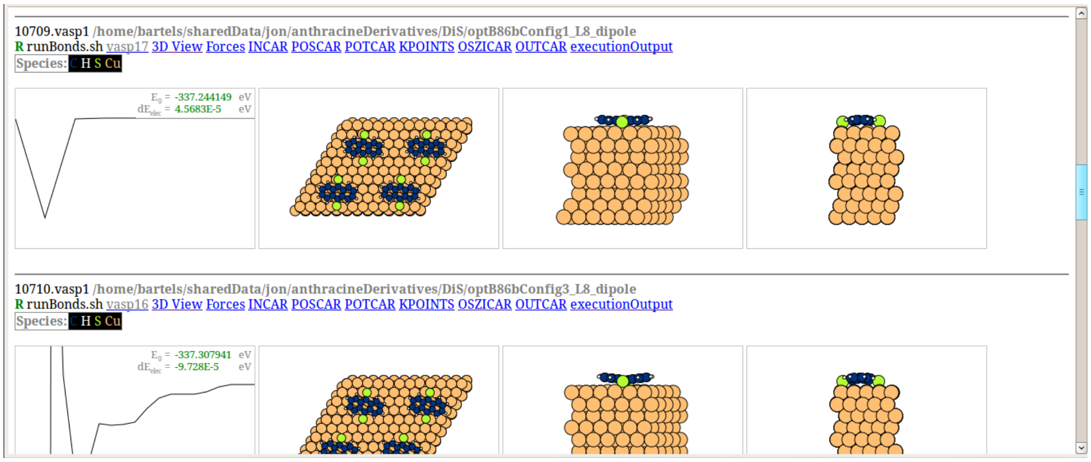

10709.vasp1 /home/bartels/sharedData/jon/anthracineDerivatives/DiS/optB86bConfig1_L8_dipole
R runBonds.sh vasp17 3D View Forces INCAR POSCAR POTCAR KPOINTS OSZICAR OUTCAR executionOutput
Species: C H S Cu

E_0 = -337.244149 eV
dE_{elec} = 4.5683E-5 eV

10710.vasp1 /home/bartels/sharedData/jon/anthracineDerivatives/DiS/optB86bConfig3_L8_dipole
R runBonds.sh vasp16 3D View Forces INCAR POSCAR POTCAR KPOINTS OSZICAR OUTCAR executionOutput
Species: C H S Cu

E_0 = -337.307941 eV
dE_{elec} = -9.728E-5 eV

Figure 1.1 Screenshot of webpage for monitoring VASP jobs.

Chapter 2

Introduction to Scanning Tunneling Microscopy (STM): interpretation and simulation of STM images

2.1 Observing Charge Density

All of the work presented in this dissertation is directly related to STM studies performed in the Bartels lab. As such it is appropriate to introduce the fundamental physical principles of operation of the STM with regards to what observables it measures and how to interpret those measurements. In what follows I will describe STMs as they specifically apply to our experiments, so for example, while an STM can be used to probe a variety of metallic surfaces (as well as other types of surfaces), I will refer to it as specifically being used to analyze a Copper surface. With that in mind, STM is an indispensible experimental tool for probing the electronic, geometric, and other physical properties of organic molecules adsorbed at the Cu (111) surface. To a good approximation, the principle observable measured by an STM is the energy-integrated electron density at any point within a 3D volume ranging from roughly 3 Å to 10 Å above the Cu (111) surface, and laterally on the orders of 10s or 100s of nm (Figure 2.1). Symbolically we can say that the measured quantity is:

$$\rho_{int}\left(\vec{r}_{tip}, V\right) = \left| \int_{E_F}^{E_F+eV} dE \;\; \rho_E\left(\vec{r}_{tip}\right) \right| , \qquad \text{(EQ 2.1)}$$

where $\rho_E\left(\vec{r}_{tip}\right)$ is the probability of finding an electron at position $\vec{r}_{tip}$ having energy *E*, *e* is the magnitude of the charge of the electron, and *V* is a supplied bias voltage which determines the energy range of integration. Absolute value signs indicate that regardless of whether *V* is chosen to be positive or negative, the integrated charge density should be a positive quantity. It is typical to denote the direction normal to the surface as the Cartesian coordinate *z*, and the coordinates in the plane of the surface as *x*, and *y* so that $\vec{r}_{tip}$ = (*x*,*y*,*z*).

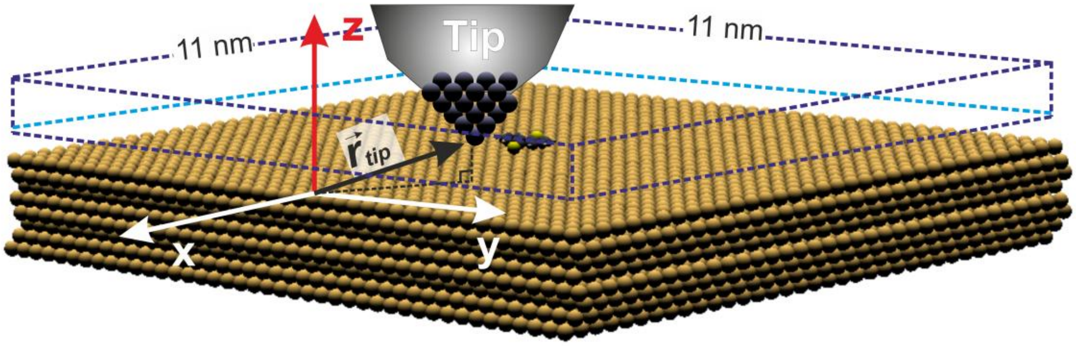

Figure 2.1 Basic setup of the tip sample junction illustrated on a Cu(111) surface with one adsorbed molecule in the scan region. Blue dashed lines indicate a typical volume in which the tip is confined, the lateral dimensions defining the chosen scan region (on the smaller side of what we typically choose).

2.2 Tip Sample Junction

To understand where the expression of equation 2.1 comes from it is necessary to consider the electrostatic setup of a typical STM scanner, which most simplistically consists of a sample (a Cu surface decorated with adsorbed molecules) and a sharp metallic tungsten (W) tip separated by several Angstroms of vacuum. Figure 2.2(c) shows a typical potential (on the left half of (c)) as seen by an individual electron under the influence of a Cu (111) surface and an adsorbed molecule; this serves as a good example of the electrostatic makeup of the sample. The potential due to the STM tip is also included on the right half of figure 2.2(c). The red line indicates the Fermi level of the sample, E_F, the highest energy occupied by an electron bound to this system at zero temperature; also shown is a red line for the Fermi level of the tip E_F^{tip}. For simplicity the potential energy surface seen by an electron has been collapsed down to 1 spatial dimension by averaging along the *x* and *y* spatial directions (dark blue graph) and separately by considering only a cut through the middle of the sample and tip (light blue graph); both ways of representing the potential lose information, given that it exists over 3-dimensional space. Classically any sample electron with energy at or below E_F should be in the potential well created by the Cu, however because of its quantum nature an electron always has a finite possibility to be observed in the regions with a potential energy higher than its energy. In particular, such an electron can be found in the vacuum region ($z > h$) above the sample: Figure 2.2(a) shows the charge density averaged in the same way as the potential, with an inset illustrating that even in regions where the charge density appears to be flat it is finite and decaying exponentially. If the electron is to be observed in this region, then some probe must be placed in proximity to the sample, resulting in an end to the potential energy barrier of the vacuum at the height where the electron is to be measured. There is therefore a finite probability that an electron can cross this barrier and enter into the probe; this is by definition the phenomenon of tunneling and is where the word tunneling in STM comes from.

The W tip is positioned above the sample (at higher *z*) so that there is still vacuum between tip and sample, and the potential created by the tip has minimal influence on that of the sample. The Cu sample is biased relative to the tip, typically so that electrons see the tip as lying at lower potential energies (right half of figure 2.2c), and we speak of the STM as having negative sample bias (electrons are repulsed from regions of lower voltage – i.e. such regions have a higher potential energy). In this configuration, a continuum of unfilled conduction band states lie above the tip's Fermi level E_F^{tip}, but below that of the sample, E_F. If the tip and sample systems were brought into direct physical contact, the vacuum barrier between them would disappear and equilibrium conditions would require that electrons flow from the sample into the empty tip states until the Fermi levels of sample and tip become equal. With the barrier held intact, only a trickle of electrons whose energies are equal to the unfilled states of the tip, are able to tunnel from the sample into the empty tip states where, due to the setup of the STM, they are transported away from the tip/sample junction. In this sense, the tip states lying between E_F^{tip} and E_F appear to remain unfilled on the timescale of electrons tunneling from the

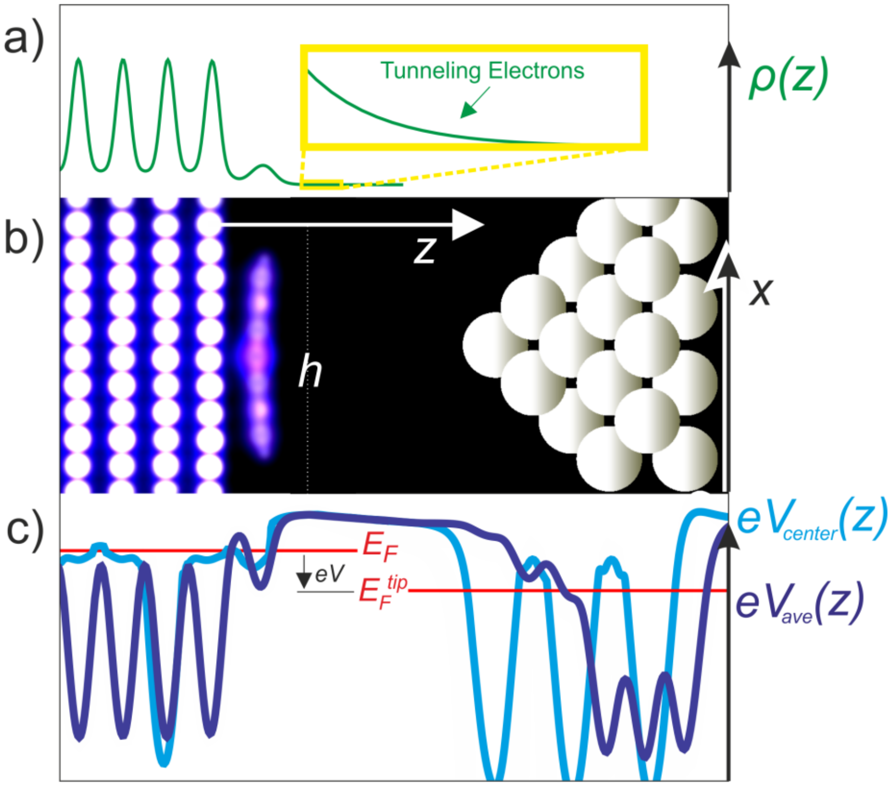

Figure 2.2 Electronic configuration of the tip-sample junction. **(a)** Total charge density of sample electrons averaged along the *x*- and *y*-directions. **(b)** Total charge density integrated along the *y*-direction (left), and hypothetical configuration of W atoms at the tip apex (right). **(c)** Dependence of the potential energy on *z* for a case of negative sample bias. These potential energy diagrams were generated using DFT calculations, though have been modified to simplify their appearance.

sample. Likewise the Cu acts as a reservoir of electrons and is easily able to replenish those that tunneled across the barrier. By amplifying the signal associated with this trickle of electrons, it is possible to detect and record a current which, by association, is called the tunneling current.

2.3 Why Tunneling Current is Proportional to Charge Density

At this point in the description, it is already possible to motivate the claim of equation 2.1. If the tip is really acting as a minimally invasive probe that registers a current every time it encounters a tunneling electron, it can be argued that the tunneling current (the true measured quantity) is proportional to the probability of finding one of the sample's electrons in the vacuum region where the tip is located, but only for those sample electrons lying between E_F^{tip} and E_F. To my knowledge there are two ways to arrive at equation 2.1 more rigorously: that due to Tersoff and Hamann[14] which centers around use of Fermi's golden rule to describe the probability of sample states transitioning into empty tip states over time, and that due to Bracher et al.[15] which reframe the problem in terms of a quantum mechanical probability current density and scattering theory. I present a brief version of the latter derivation in appendix A for reference.

2.4 Imaging

Based on the derivation provided in appendix A, under the assumption of a delta-function tip, the tunneling current measured by the STM should therefore be given as

$$I \propto \int_{E_F}^{E_F+eV} dE \;\; \rho_E(\vec{r}_{tip}) \,, \qquad \text{(EQ 2.2)}$$

where again, $\vec{r}_{tip}$ is the location of the tip. Under ordinary operation, the position $\vec{r}_{tip}$ is raster scanned along the *xy*-plane (the plane of the substrate surface) while the current I is continually measured. A feedback control loop is implemented via digital signal processing (the analog current signal is converted to a digital representation, processed, and then the feedback response is converted to an analog voltage signal) to maintain constant current at a desired set-point by adjusting the tip's *z*-position relative to the surface. If the measured current exceeds the set-point (in magnitude), then *z* is increased: the exponential drop-off of electron density into the vacuum (inset of figure 2.2(a)) above the sample guarantees that a lower current will be achieved. Similarly, if the measured current falls below the set-point, then *z* is decreased. In this way, a surface of constant integrated charge density is traced out by the tip as it rasters the sample (figure 2.3).

The *z*-coordinate of the tip is recorded for each *x*,*y* position so that a map of the surface of constant integrated charge density (or iso-surface) is created. Typically this map is displayed as a grayscale image in which positions with higher *z* are displayed as closer to white on the grayscale spectrum while positions with lower *z* are displayed as closer to black on the grayscale spectrum (see figure 2.3). Figure 2.3 is slightly misleading in that true STM scans are typically done over a square or rectangular region (neglecting imperfections in the mechanics of rastering a tip at slightly fluctuating temperatures over scales on the order of 10s or 100s of nm); however, the calculated images (as presented in the figure) will necessarily take on the shape of the repeated unit cell (VASP calculations are performed under periodic boundary conditions).

2.5 Simulating an STM Image

The first level of simulation of an STM image occurs in the mind of the researcher performing a scan of a given sample. By just looking at an image we can predict that regions that are lighter in color represent one of two possibilities: either 1) the region is physically higher than its surroundings so that the charge density iso-surface will also necessarily be physically higher in that region, or 2) the region might be roughly the same height as its surroundings but contains a higher charge density (i.e. it is somehow chemically different) in which case the charge density iso-surface must deform upward around that region of higher density. We can come to the opposite conclusions for regions in an STM image that are darker than their surroundings. All of this comes with the caveat that because we do not necessarily know the precise nature of the tip (for example has a molecule desorbed from the sample and attached itself to the tip?), the details of how it interacts with the underlying sample may vary in misleading ways.

So, not necessarily trusting our first intuition, or perhaps just wanting some deeper insights into the details of what is being observed, the next step is to simulate an STM image with a computer. Figure 2.3 illustrates that the process of simulating an STM image in this way is, under ideal conditions, as simple as mapping out a surface of constant integrated charge density, roughly associated with some height above the Cu surface. The integrated charge density (in the form of a 3D array) is a readily available output quantity from VASP in a text file called PARCHG, so long as we restrict ourselves to approximate the energy range (E_F to $E_F + eV$)

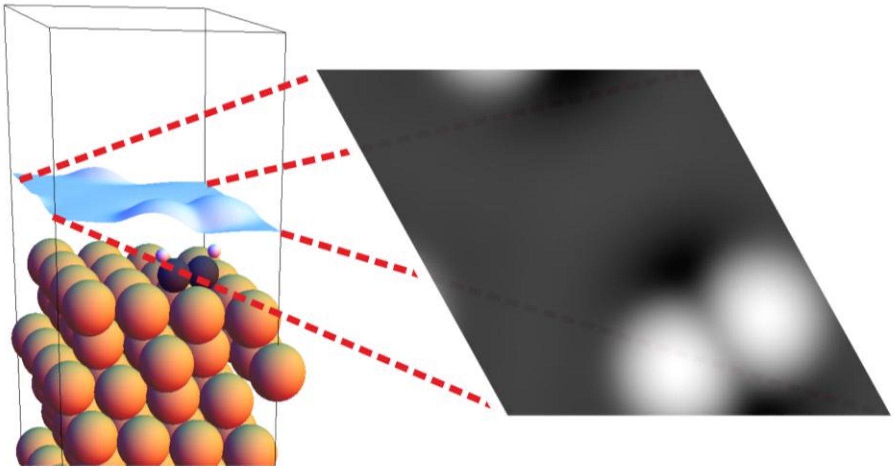

Figure 2.3 Iso-surface of integrated charge density above a sample containing an adsorbed acetylene molecule, illustrating how the iso-surface is converted to a gray-scale image.

as being a range of KS energy eigenvalues rather than true energies (empirically it can be seen that this approximation works quite well, see e.g. Chapter 3).

There are, however, many imperfections in a real system (and with the approximations made thus far) which may need to be accounted for in some way. One immediate problem is that, while we know that the tip traces out an iso-surface, we do not know which iso-surface (i.e. which specific charge density) to trace out. Using the knowledge of reasonable tip-sample distances indicated previously, we can find the charge densities associated with such distances above a clean Cu surface (as calculated by DFT), and use those values as a set of iso-surfaces to generate simulated images for, and then compare to the actual experimental images.

Furthermore, it should be expected that under ordinary experimental conditions there are vibrations which effectively cause the precise location of the tip relative to the sample to be "blurred" on time-scales faster than data recording (e.g. zero-point vibrations) and slower than data recording (e.g. mechanical vibrations of the STM vacuum chamber and surrounding environment). Additionally, as pointed out in appendix A, the precise geometric and electronic makeup of the tip is unknown, so that the assumption of a point-like delta-function tip may not be appropriate. I find that many of these issues can be addressed on a phenomenological level by replacing point-like sampling of the integrated charge density with sampling of a Gaussian or multiple Gaussian's about the tip position (this should help account for vibrations on timescales faster than the STM sampling rate as well as the unknown, but presumed, electronic and geometric features of the tip) and additionally post-processing the simulated images with Gaussian blurs (which should help to account for vibrations on time scales slower than the sampling rate – in fact, on the experimental side of things, raw STM images in particular are often blurred/smoothed in post processing in an attempt to improve image quality). The success of this phenomenological technique is apparent in the high level of agreement between the simulated and experimentally acquired images of Chapter 3, and can even lead to a better understanding of the makeup of the tip itself.

Chapter 3

Acetylene on Cu(111): Imaging a Molecular Pattern with a Constantly Rearranging Tip

3.1 Abstract

Acetylene on Cu(111) is investigated by scanning tunnelling microscopy (STM); an adsorption pattern previously derived from diffraction measurements can be validated, if the variation of the STM image transfer function through absorption of an acetylene molecule onto the tip apex is taken into account. Density functional theory simulations point to a balance between short-range repulsive interactions of acetylene/Cu(111) associated with surface stress and longer range attractive interactions as the origin of pattern formation.

3.2 Introduction

Acetylene is one of the platform chemicals of today's chemical industries; innumerable everyday compounds as well as specialty use ones can be traced to acetylene as a foundation feedstock.[16] A significant portion of the processes by which these are made relies on heterogeneous catalysis, and copper is a metal found in many industrial catalyst compositions. This renders understanding the interaction of acetylene with the thermodynamic equilibrium (111) surface of copper an obvious goal. Furthermore, acetylene is one of only a few (organic) molecules with 4 atoms or fewer and thus presents an excellent model system to study fundamental metal-organics interactions at limited complexity. In this manuscript, we describe real-space scanning tunnelling microscopy (STM) investigations of acetylene on Cu(111) and apply density functional theory (DFT) modelling to elucidate the particular STM imaging mode in the presence of an acetylene molecule at the tip apex.

Prior investigation revealed that acetylene adsorbs on Cu(111) with its carbon-carbon bond lying across a bridge site [17, 18] and with its hydrogen atoms each pointing away from the surface as shown in figure 3.1(a), in contrast to the linear character of acetylene in the gas phase. Isolated acetylene molecules have been imaged on Cu(111) by Konishi et al. [19] and on Cu(100) by Stipe et al. [20]. At higher coverage, reciprocal space data, i.e., low energy electron diffraction (LEED) [2], indicates a $\begin{pmatrix} 2 & 1 \\ 0 & 4 \end{pmatrix}$ pattern, in which two molecules at different rotational orientations are found in each unit cell (figure 3.2(a)). This work provides real-space validation of this pattern and explores fundamental aspects of the acetylene substrate interaction.

Imaging acetylene coverages on Cu(111) we find a pronounced sensitivity of the STM image to the tip condition in a very particular way: acetylene is found to form rows of molecules, as predicted by LEED, but the contrast between adjacent rows varies considerably,

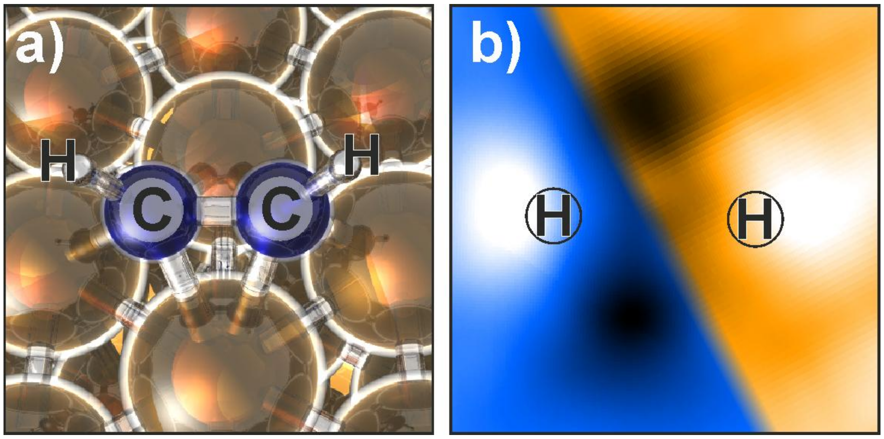

Figure 3.1 (a) DFT-simulation of acetylene adsorbed on a Cu(111) bridge site. **(b)** simulated image (bottom left, blue) and STM image (top right, orange) of an isolated acetylene molecule on Cu(111) highlighting the good correspondence between simulations and measurement; STM Parameters: Bias = -1.9 V, Current = 0.1 nA, Image Size = 8 Å x 8 Å.

sometimes making them appear practically identical, sometimes fundamentally different. This prevents direct correlation between an STM image and any particular adsorption structure; no information on the molecular orientation or registry in neighboring adsorption rows can be obtained in a straight-forward way from STM images. Using DFT modelling of the adsorption configuration, we are able to show that the particular imaging contrast is caused by attachment of an acetylene molecule to the STM tip apex in a fashion that allows it to adjust itself dynamically to the orientation of the substrate acetylene rows directly underneath the tip, thus generating an image transfer function sensitive to the local rotational orientation of the surface pattern.

Variation of imaging conditions induced by the transfer of non-metallic species on the tip apex was first reported two decades ago by Eigler's group in the context of experiments in which Xenon atoms acted as atomic switches.[21, 22] Molecular adsorption has been shown by Rieder's group to provide chemically sensitive contrast[23] and, since then, numerous contrast modes in STM based on related phenomena have been reported.[24-26] We believe that these

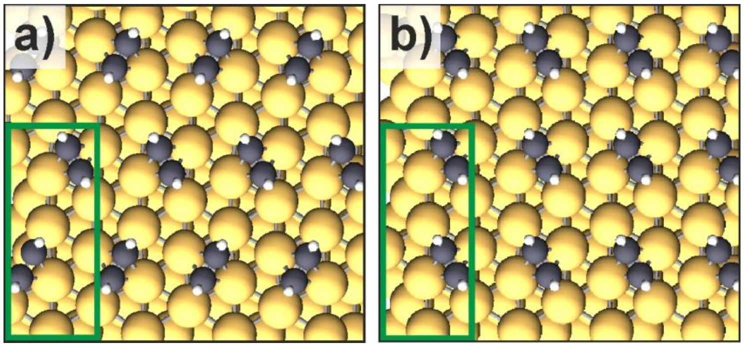

Figure 3.2 (a) adsorption geometry of acetylene on Cu(111) as predicted from LEED measurements [2]; **(b)** alternative adsorption geometry potentially compatible with STM images. The green boxes in **(a)** and **(b)** are the supercells used in calculations.

findings for acetylene are distinct to the extent that they involve dynamic reorientation of the molecule at the tip apex in a fashion determined by and sensitive to the orientation of the substrate adsorption pattern. Modelling this behaviour, we can achieve high-fidelity agreement with the images obtained by STM, confirming the predictions from LEED measurements in real space and ruling out the presence of alternative adsorption patterns.

3.3 Experimental Setup

All STM measurements proceeded on a Cu(111) substrate cleaned by cycles of sputtering and annealing. The cleanliness of the sample was ascertained by imaging at ~85K followed by exposure to 10^{-8} Torr for 1.5 minutes (~ 0.9 Langmuir) of acetylene (99.6% pure, Airgas) on the cryogenic sample. Immediately following exposure, the sample was allowed to warm to room temperature over 45 minutes for annealing of the adsorbate coverage, and then re-cooled for imaging.

DFT calculations use the VASP code[27-30] with the Generalized Gradient Approximation (PBE-GGA) [31, 32] for the exchange-correlation functional and a projector-augmented-wave (PAW) basis[33, 34]. All results are optimized so that the remaining forces are less than 0.03 eV/Å. Simulations of STM images use a 6 layer slab separated by 23 Å of vacuum in the same supercell as figure 2a on a 13 × 7 × 1 k-point mesh with plane wave and augmentation charge energy cutoffs of 600 and 2000 eV respectively. Calculations to assess acetylene-substrate interactions use different supercells and k-point meshes as indicated below.

3.4 Results and Analysis

Figure 3.3 shows a selection of STM images acquired on a sample with 1/4 monolayer (ML) acetylene (with 1 ML taken as one adsorbate per substrate atom). Depending on the tip condition, the parallel rows of protrusions appear to have either identical or different heights.

These images pose two questions: a) can the rows observed by STM be identified as a pattern of molecules aligned in parallel in each row but featuring alternating orientation in neighbouring rows as predicted by the LEED data (figure 3.2(a)) [2], thus ruling out an alternative pattern of identically aligned molecules (figure 3.2(b)), and b) why is it that in some cases the molecular rows are imaged identically while in others a pronounced difference is observed.

3.4.1 Pattern identification by STM image simulation

We first address whether the pattern of figure 3.2(a) is actually capable of producing the variety of images we observe in STM, of which a subset is shown in figure 3.3. Clearly a sharp metallic tip cannot provide the variation in contrast between neighbouring rows that is observed. Thus, we explore the imaging properties of an STM tip decorated with an acetylene molecule at its apex, a likely occurrence when scanning an acetylene-covered substrate. Here it is important to consider the image of an isolated acetylene molecule (figure 3.1(b)), which consists of two areas of high tunnelling probability separated by ~2.5 Å while the remainder of

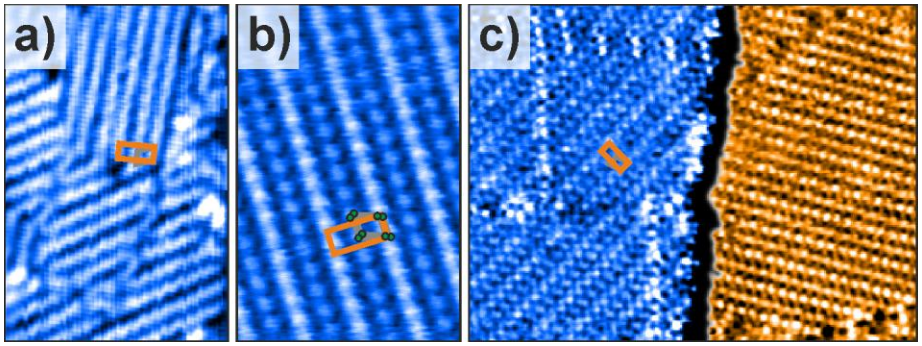

Figure 3.3 1/4 ML coverage of acetylene on Cu (111). STM Parameters **(a)**: Bias = -1.07 V, Current = 96 pA, Image Size = 6.2 nm x 9.3 nm. **(b)** Bias = -0.66 V, Current = 0.11 nA, Image Size = 4.2 nm x 6.3 nm. **(c)** Bias = -1.07 V, Current = 0.11 nA, Image Size = 16.7 nm x 12.5 nm. Differences in the appearance of (a), **(b)** and **(c)** are due to tip conditions to be discussed. Adsorption positions of the acetylenes are shown in **(b)** with circles representing the carbon atoms connected by a parallelogram (grey). The unit cell is indicated with a rectangle (orange).

the molecule has lower (or similar) tunnelling probability than the underlying substrate. In the s-wave approximation of the Tersoff and Hamann interpretation of the STM current signal [14], the STM tip contours a surface of constant charge density integrated between the tip's and the surface's Fermi level (whose difference is given by the applied bias). This approximation has been shown to be successful in many cases, yet to be lacking for cases with more complex interaction between substrate and adsorbate electronic states.[25, 35-38]

Tersoff and Hamann showed that under the assumption of an s-type wave function at the tip apex, the surface of constant energy-integrated charge density can be determined by treating the tip as an infinitely sharp point. This approach can be amended straightforwardly to the case that an acetylene molecule is attached at an in-plane angle ϕ and an out-of-plane angle θ to the tip: rather than sampling only at one point, we sample the calculated charge density with a pair of Gaussians spaced apart like the apparent height maxima of an acetylene molecule on Cu (111) oriented in space according to the angles ϕ and θ. Figure 3.4(a) shows an example: the (orange) centre part of the image was acquired by STM and the (blue) sides of the panel are simulated STM images using the acetylene configurations on the tip apex shown in the left and right of the panel. In both cases the acetylene molecule is titled by $\theta = 4°$ relative to the substrate but its rotational orientation on the tip apex differs by 60°. Recognizing the different adsorption geometry of the acetylene molecule is tantamount to obtaining meaningful correspondence between experiment and modelling: using a standard s-state (point-like) tip, the image of figure 3.4(b) is obtained; modelling the left part of figure 3.4(a) with the same orientation of the tip acetylene molecule as on the right, the image of figure 3.4(c) is obtained; using the adsorption pattern of figure 3.2(b) with the same tip conditions as the left of panel yields the image of figure 3.4(d). Neither figure 3.4(b) nor 3.4(c) is a faithful representation of

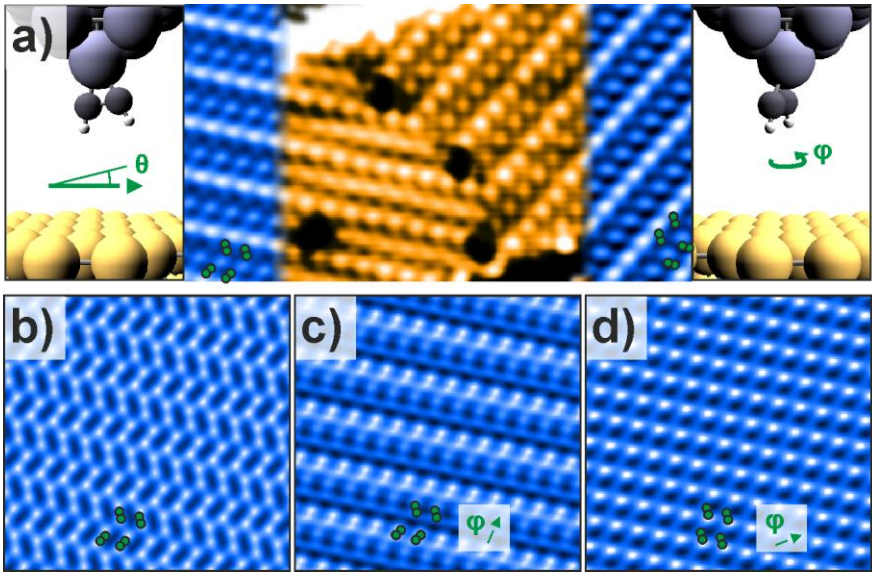

Figure 3.4 (a) The centre panel (orange) shows an STM image of a boundary between two rotational domains of an acetylene coverage on Cu(111), which is at the left and right edge continued (blue) with simulated STM images using the tip geometries shown on the respective sides; Tip Parameters: θ = -4° (left) +4° (right); STM Parameters: Bias = -1.1 V, Current = 0.10 nA. **(b)** The pattern on the left of (a) modelled with a point-like tip. **(c)** The same pattern, but with an adsorbed acetylene at the same angle ϕ ~ 25° (as measured from the panel vertical) used on the right of panel **(a)**. **(d)** The pattern of figure 3.2**(b)** under the same conditions used to generate the left of panel **(a)**: ϕ ~ 70°.

the rotational domain on the left of panel a, and the image of figure 3.4(d) associated with the alternative adsorption pattern (figure 3.2(b)) is not seen experimentally. As the STM image in panel (a) was scanned in horizontal lines, this finding implies that not only was an acetylene molecule present at the tip apex, but also that it reoriented itself in response to the substrate pattern alignment in every scan line at high fidelity.

This approach to simulating STM images is not limited to the particular pattern observed in figure 3.4(a). We repeated this procedure for a wider range of STM images obtained than the sampling in figure 3.3 and were in each case able to obtain convincing correlation. Figure 3.5 shows two additional examples. The pattern in figure 3.5(a) corresponds to figure 3.3(a) and can clearly be modelled at high fidelity using a horizontal acetylene molecule (θ = 0°) at the tip apex.

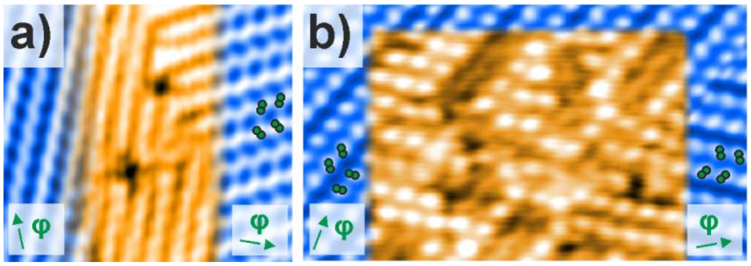

Figure 3.5. Comparisons between STM images (centre, orange) and model (sides, blue). (a) Model Parameters: θ = 0°; STM Parameters: Bias = -0.66 V, Current = 0.11 nA. (b) Tip Parameters: θ = 45°; STM Parameters: Bias = -0.99 V, Current = 0.10 nA.

In contrast, the rather disordered pattern in the centre of figure 3.5(b) is faithfully extended using a tilted acetylene molecule (θ = 45°) on the tip.

3.4.2 Identification of substrate strain as determining adsorption pattern

Having validated that the images of acetylene/Cu(111) are indeed consistent with the predicted $\begin{pmatrix}2 & 1\\0 & 4\end{pmatrix}$ acetylene pattern, we turn to the origin of the different orientations of the acetylene species in each unit cell. To this end, we compare DFT simulations of both adsorption configurations of figure 3.2 in supercells of identical size and geometry. Comparison between systems, in which the molecules are attached and lifted from the substrate yields a binding energy per acetylene molecule of 2.35 eV for the structure predicted by LEED (compared to 2.29 eV for the configuration of figure 3.2(b)), providing an energetic explanation for this preference.

In both supercells the molecules are sufficiently separated from one another (~ 5 Å) that their interaction has to be dominated by substrate-mediated components. Prior work showed that acetylene adsorption induces stress in a Cu(111) surface that is directed perpendicular to the molecular axis, attempting to widen the span of the bridge site the molecule inserts itself into [39]. Using 3 atoms thick copper slabs in our calculations, we find that indeed the system is under compressive strain. Allowing the supercell to artificially expand to equilibrium (which in reality would be forbidden through interaction with the underlying bulk), the energetic difference between the patterns of figures 3.2(a,b) vanishes to < 1 meV, i.e., beyond the expected resolution of our calculations. In this process, both patterns expand by nearly the same amount (1% and 2% along the short direction and long direction as indicated in figure 3.2, respectively). Thus, the energetic difference between the two adsorption patterns can be attributed to differences in the resultant compressive stress on the lattice; it is energetically unfavourable when all molecules are aligned in parallel and their stress vectors add up.

3.4.3 Aggregation of acetylene molecules due to long-range substrate mediated interaction

Assignment of the adoption of the observed surface pattern to release of surface stress poses the question whether the ordering of the molecules into the patterns of figure 3.2(a)/figure 3.3 is solely governed by repulsive interactions. While ordering based on repulsive intermolecular interactions is conceptually possible in the presence of the dominant interaction anchoring the molecules to the substrate, it generates a more tenuous foundation for large scale order, as any set of vacancies is not expelled to the outside of the adsorption pattern. To

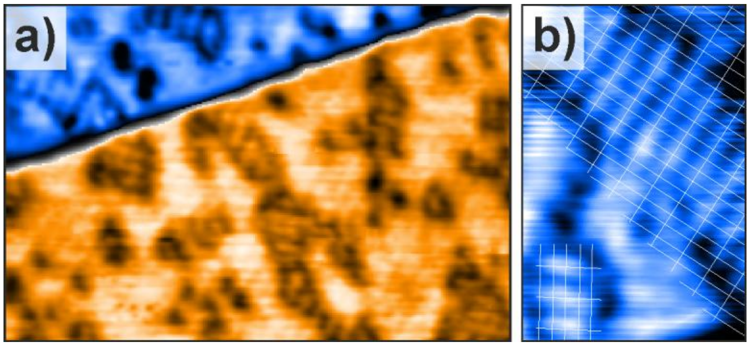

Figure 3.6. Acetylene at ~1/8 ML coverage on Cu (111). **(a)** Island formation is observed. **(b)** The islands are composed of rows of molecules of the same periodicity found at elevated coverage, indicated here with white grid lines. STM Parameters **(a)**: Bias = -0.83 V, Current = 0.10 nA, Image Size = 16 nm x 11 nm. **(b)**: Bias = -1.0 V, Current = 0.12 nA, Image Size = 3.9 nm x 5.8 nm.

investigate whether net attractive interactions between adjacent acetylene molecules also exist on Cu(111) we prepared incomplete coverages (figure 3.6, ~1/8 ML acetylene). Here acetylene molecules aggregate into small islands and, more frequently, into patterns of adjacent rows, that feature the same periodicity found at 1/4 ML coverage (figure 3.6(b)). The formation of such aggregates indicates the presence of attractive interactions. Thus, in addition to the surface stress that orients the molecules in dissimilar orientations, there are also attractive interactions between the molecules present. Given the comparatively large intermolecular distance in this pattern, these interactions need to be mediated by the substrate.

Rieder's group and others have shown [4, 40-55] that the substrate is capable of mediating attractive forces over distances far greater than the size of individual atoms or molecules. Following Ref. [53], we test whether the variation in total system energy *E'* between different configurations of acetylene molecules on Cu(111) can be described by the sum of substrate-mediated pair interactions: $E^{'} = \sum_r E_{pair}\,(r)$, where *r* ranges over the set of all pair-wise distances between acetylene molecules on the surface. For such systems a pair interaction energy function (expression for $r > r_5$ of equation 3.1) has been proposed [56], where *A* represents the overall interaction amplitude, its Fermi wavelength of π/ k_F, *δ* the backscattering phase shift of each atom and *r* the pair distance. This approach is unable to describe short-range interactions correctly, which are important for the pattern formation. To account for this we define a set of 5 shortest distances $\{r_i\}$={1, √3, 2, √7, 3} × 2.55 Å for which E_{pair} is defined explicitly:

$$E_{pair}\,(r;\{\varepsilon_i\},A,k,\delta) = \begin{cases} \varepsilon_i, & if\ r = r_i, i \leq 5 \\ \dfrac{A\sin(2k_F r + 2\delta)}{r^2}, & if\ r = r_i, i > 5\,. \end{cases} \qquad \text{(EQ 3.1)}$$

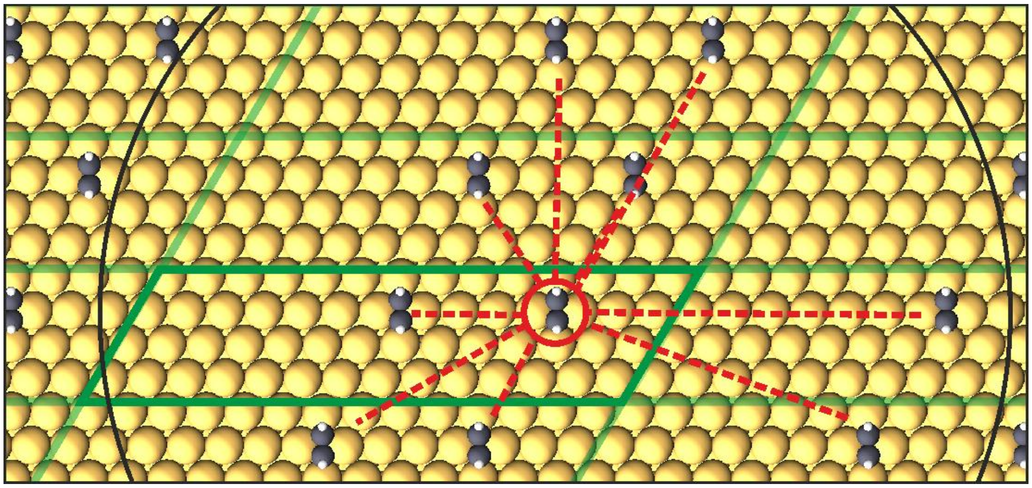

Figure 3.7 Setup for calculation of the surface state mediated interaction. Dashed red lines indicate the pair interactions. A black circular outline indicates the cutoff radius of 30 Å used. For simplicity, only the interactions for the circled acetylene are shown, and only those interactions between acetylenes visible in the frame.

In order to test whether such an interaction may cause the ordering of acetylene into the row patterns we calculated the total energy of 24 different relative locations of two acetylene molecules on 14 × 4 × 3 copper atoms slabs (figure 3.7 shows an example). To limit configurational and computational complexity, we only considered molecules in the same orientation on the surface and one k-point, respectively. Depending on the intermolecular spacing, we find a variation of the total energies by ~0.1 eV with the exception of the case for directly adjacent acetylenes (separated by one substrate atomic spacing only), for which the total energy is higher (less favourable) by ~0.6 eV.

We find the interaction potential E_{pair} by fitting its 3 variables and 5 explicitly defined values to achieve a best match of E' for all 24 supercell geometries considered simultaneously. Here we include interactions between acetylene molecules and their copies in neighbouring unit cells up to a distance of 30Å (figure 3.7). The optimal values for the parameters are A = 2.1 eV, k

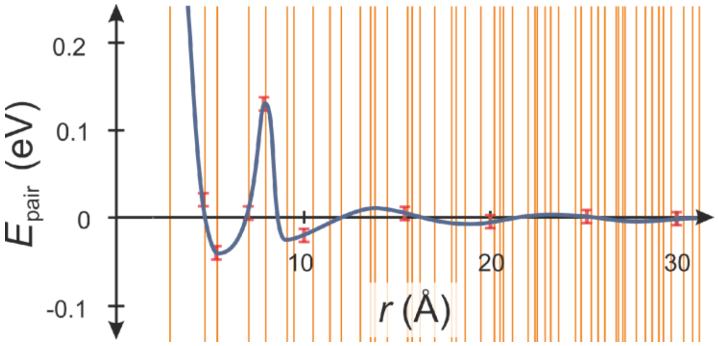

Figure 3.8 Interaction potential E_{pair}. Vertical lines indicate distances sampled. The error bars correspond to ~ ±0.01 eV fit error.

= 0.33 $Å^{-1}$, δ = 0.7 π. The resulting interaction potential is shown in figure 3.8; the vertical lines indicate the intermolecular separations present in our set of relative acetylene locations. By evaluating the rms error in the fit of the set of 24 configurations, we can estimate the error band of our fit. Figure 3.8 reveals a pronounced (~0.05 eV) attraction at separations of ~ 5 Å, the intermolecular spacings in the experimentally observed pattern, followed and preceded by repulsive interactions. Given that only molecules of one orientation were considered, the particular separations found at molecules in neighbouring rows of 5.6 Å was not tested explicitly but falls into the attractive region of E_{pair}.

The optimal fit value of the periodicity k of 0.33 $Å^{-1}$ is in reasonable agreement with the sp-band and surface-state Fermi wave vectors on the Cu (111) surface of 0.26 $Å^{-1}$ and 0.22 $Å^{-1}$ [57], respectively. In Rieder's and other's work [4, 40-55] long range interactions on Cu(111) were ascribed to the surface state and it is also a likely candidate here. However, including only 3 substrate layers in our simulations (although resulting in >160 substrate atoms per supercell investigated) does not allow us to distinguish between the sp-band and surface state: as shown by Berland et al., [58] the surface states on the top and bottom of a slab can only clearly be distinguished from the bulk states and one another with a minimum of 6 copper layers (and only then with appropriate transformations of the Kohn-Sham states). Consequently, our simulations do not permit direct attribution of this effect to the Cu(111) surface state. Experimentally, the propensity for acetylene to form odd-shaped aggregates prevents a meaningful analysis of STM images by pair correlation function to obtain experimental verification of the parameters of E_{pair}. Nevertheless, the data of figure 3.8 is a clear indication that acetylene adsorbates generate a net attractive interaction between species at a certain distance, despite causing a compressive strain on the top substrate layer.

3.5 Conclusion

We have shown that validation of a diffraction-derived surface pattern [2] of acetylene on Cu(111) by STM is possible, if the modification of the STM image transfer function through the adsorption of an acetylene molecule onto the tip apex is taken into account. In that case, the images of acetylene patterns on Cu(111) also include direct evidence of the rotational orientation and dynamics of the acetylene species attached to the tip apex. DFT modelling of acetylene/Cu(111) reveals that the molecular orientation and separation is governed by a balance of repulsive interactions associated with stress induced in the top surface layer and attractive interactions mediated by the electronic structure of the substrate. Computationally relatively inexpensive modelling of the substrate with 3 layers allows one to obtain the periodicity of the intermolecular interaction that is in reasonable agreement with experimental values of the band structure of copper.

Chapter 4

Anthraquinone Network – Part 1

Do Two-Dimensional "Noble Gas Atoms" Produce Molecular Honeycombs at a Metal Surface?

4.1 Abstract

Anthraquinone self-assembles on Cu(111) into a giant honeycomb network with exactly three molecules on each side. Here we propose that the exceptional degree of order achieved in this system can be explained as a consequence of the confinement of substrate electrons in the pores, with the pore size tailored so that the confined electrons can adopt a noble-gas-like two-dimensional quasi-atom configuration with two filled shells. Formation of identical pores in a related adsorption system (at different overall periodicity due to the different molecule size) corroborates this concept. A combination of photoemission spectroscopy with density functional theory computations (including van der Waals interactions) of adsorbate-substrate interactions allows quantum mechanical modeling of the spectra of the resultant quasi-atoms and their energetics.

4.2 Introduction

Since Eigler's group and others imaged the surface state oscillations on (111) surfaces of coinage metals[59-61] and showed that they can be confined in corrals set up from adsorbed atoms or molecules[62-65] two decades ago, their aesthetic appeal and fundamental physics have captivated the general public and surface scientists alike. In the meantime, evidence has been found that surface state scattering mediates inter-adsorbate interactions that favor particular separations or atomic patterns.[1, 42, 43, 45, 47, 48, 50-54, 66-69] Here we show results that arguably close the circle begun with the formation of quantum corrals: the self-assembly of molecules into a regular porous network driven by optimization of the electronic quantum dot character of the surface state inside the pore. Thus, we find that quantum corrals, originally painstakingly assembled one atom at a time, can self-assemble in a molecular system driven by optimization of the quantum dot character of the enclosed electrons. While the effect of confinement on electronic states has been noted often, the idea that closed-shell "noble-gas"-like configurations have greater stability represents a new ordering principle in surface science. Molecular pores at surfaces can in turn serve to elucidate fundamental physics of adsorbates in confinement, as shown in refs. [5, 6, 70]

Anthraquinone (AQ) molecules adsorb on Cu(111) into a molecular network that spans pores of ~4 nm in diameter (figure 4.1(a)). This network is stable up to ~190K. Underlying the formation of AQ chains and pinwheel vortices are attractive, short-range hydrogen bonds, which were measured to be ~50 meV,[71] i.e. ~100 meV per AQ-AQ bond; a very crude quantum chemical calculation gave a number of the same magnitude.[63, 72] When we originally encountered this network,[1] we ascribed its formation to a competition between these attractions and an unspecified long-range force preventing aggregation into a compact pattern. Strikingly, this network is not only open but also very regular, suggesting that the effect causing pore formation favors one specific pore shape and size (a regular hexagon with 3 molecules per side): pores that have more or fewer than three molecules on any of their sides are typically present only to accommodate molecules pinned at surface defects such as step edges. A possible explanation of the observed size makes use of the oscillatory interaction mediated by the surface state on Cu(111),[73] which is much longer range than the analogous interaction mediated by bulk states.[52, 72, 74, 75] Monte Carlo simulations based on this perspective in a simplified model could account generically for some of the experimental observation but were not fully satisfactory.[76] Also, at very low coverages only straight molecular rows are formed; virtually no vertices can be found suggesting that their presence is stabilized by the pore formation.

Lobo-Checa et al.[77] found that confinement of the surface state in a molecular network through scattering from organic molecules[78] can give rise to quantized electronic states, a concept further explored by Barth's group[79] and related to speculations about the stability of islands in metal epitaxy.[80] Given the high mobility of AQ on Cu(111),[71, 81] we suggest that optimization of the electronic structure of the confined surface electrons, as 2D

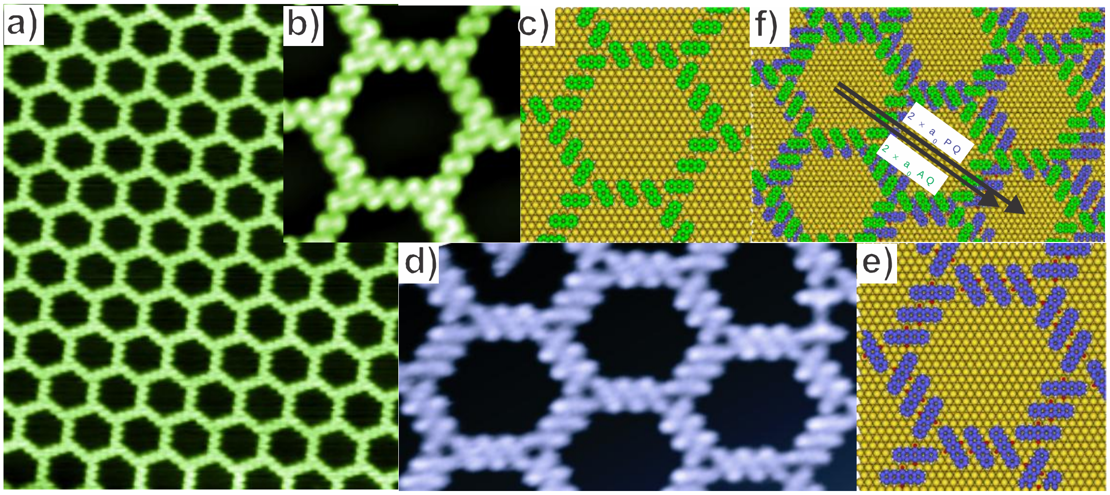

Figure 4.1 (a) STM image of regular AQ network. Image parameters: 26 nm × 29 nm; Bias –2.53 V; Current 0.05 nA. (**b,c**) Single pore of AQ (image parameters: 7.4 nm × 7.4 nm; Bias –2.4 V; Current 0.08 nA) and corresponding model. (**d,e**) PQ pores (image parameters: 19 nm × 9 nm; Bias –3.8 V; Current 0.01 nA) and corresponding model. (**f**) Superposition of PQ and AQ networks. The arrows show that the periodicities of the AQ and PQ networks differ substantially but their pore sizes are the same.

quantum dots with a closed-shell orbital configuration, is the foundation for the porous ordering of these films. In support of this proposition we find the formation of a network with virtually identical pores by substantially larger molecules (pentaquinone, PQ), requiring a different superlattice periodicity.

4.3 Methods

In this work we present a combination of scanning tunneling microscopy (STM) and angle-resolved ultraviolet photoemission spectroscopy (ARUPS) data with theoretical modeling. All experiments use Cu(111) samples prepared by multiple sputtering and annealing cycles followed by deposition of AQ or PQ from a glass capillary. Synchrotron ARUPS experiments were conducted at beamline 7.0.1 of the Advanced Light Source using a gradient coverage created by gradually removing a shutter between deposition source and sample; STM experiments use homogeneous coverages. Deposition occurred on a cryogenic sample, and imaging proceeded after annealing to room temperatures. The modeling of the coupling between the molecular overlayer and the copper surface was based on density-functional theory (DFT) calculations using the PBE[31] functional with the ultrasoft pseudopotential code DACAPO[82] and including van der Waals interactions via the vdW-DF2 exchange-correlation functional.[83, 84]

4.4 Results and Analysis

In order to understand the effect of molecular network formation of AQ on the Cu(111) surface state, we model its confinement inside the pores not only for the experimentally observed pore geometry but also for all other pore shapes that can be created from AQ vertices and rows (even for pore shapes incompatible with continuous tiling of the surface). Based on the threefold symmetry of Cu(111), we begin with the eigen-functions of a particle-in-a-triangular-box, which we relax into the pore boundary drawn by the locations of those AQ carbon and oxygen atoms adjacent to the pore interior;[78] we find the resultant energy spectrum. Appendix B includes an excerpt from a table of the properties (spectrum, geometry, eigenstates, etc.) of the 85 pores considered (the full table can be found in the supporting material for this published work [4]); for reasons of practicality, we limit our survey to pores whose longest molecular row is 6 or fewer units long.

The Cu(111) surface state's band bottom E_0 (relative to the Fermi energy E_F) and its effective electron mass m have been established through ARUPS. [85, 86] On a bare Cu(111) surface the surface state contains only a fraction γ of an electron per substrate atom, where

$$\gamma = \frac{m|E_0|A_0}{\pi\hbar^2},$$

with A_0 the area per atom on Cu(111), i.e., the surface state Fermi wave vector describes a circle much smaller than the surface Brillouin zone.

From the area enclosed by each pore, we can thus learn how many electrons the spectrum of the pore has to accommodate below E_F. Taking zero energy at our experimental surface state band bottom of -418 meV, we find that the electronic spectra of all possible pores have fewer levels below E_F than needed. Figure 4.2(a) plots this deficit (Δn) for all pores investigated in order of increasing pore area; it shows significant modulation since it depends on whether there are pore states just above or just below E_F. Again, all pores show an electron deficit.

Confinement of surface states is, however, not the only effect of AQ adsorption. In the simplest picture, AQ adsorption increases the surface dipole (due mainly to charge transfer to the more electronegative quinone), increasing the work function and shifting E_0 up (relative to E_F). We explored this phenomenon both experimentally by ARUPS and theoretically. Measuring

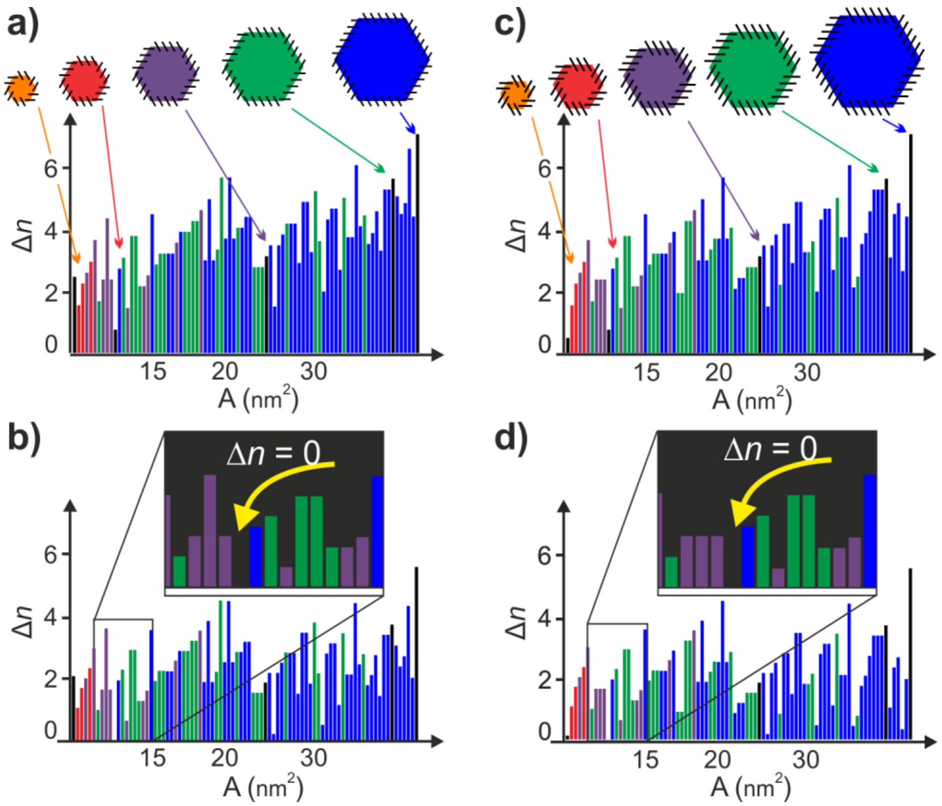

Figure 4.2 Graphs of electron deficit *Δn* for (**a**) AQ pores with no E_0 shift, (**b**) AQ with the experimentally determined E_0 shift included, **(c, d)** equivalent plots for PQ. The pores are listed in order of increasing enclosed area, with regular hexagons shown in black. Colors indicate the number of molecules on the longest side of a given pore (brown is 2, red is 3, purple is 4, green is 5, and blue is 6).

the surface state dispersion on a sample as a function of the position in a gradient coverage, we find the position of the band bottom relative to E_F as a function of the coverage (figure 4.3) similar to Scheybal et al.'s work on pentacene.[87] Unlike the molecular system of Lobo-Checa, et al.,[77] which can only assemble in one porous fashion, our ARUPS spectra do not show individual pore states, because several geometric factors prevent a dominant fraction of any crystal from being covered with a perfect AQ network. DFT modeling is only possible at or near the high coverage limit, because of the large slab thickness (at least 6 layers of Cu) required to model the surface state adequately. The green data points in figure 4.3 correspond to calculations for parallel AQ rows separated by 0, 1, 2 substrate atomic spacings (3×5, 3×6, and 3×7 atoms supercells and attach seamlessly to our experimental dataset.

If the sole effect of AQ adsorption were the field due to the enhanced surface dipole, we would expect a linear dependence on coverage. This is qualitatively seen in figure 4.3; to avoid prejudication of our model, we use a five-point-average fit to guide the eye; some nonlinearity is to be expected related to differences in the local geometries and sample quality.

Different-size pores correspond to different AQ coverages and, thus, different E_0. This, in turn, changes the fraction of the surface Brillouin zone corresponding to the occupied surface

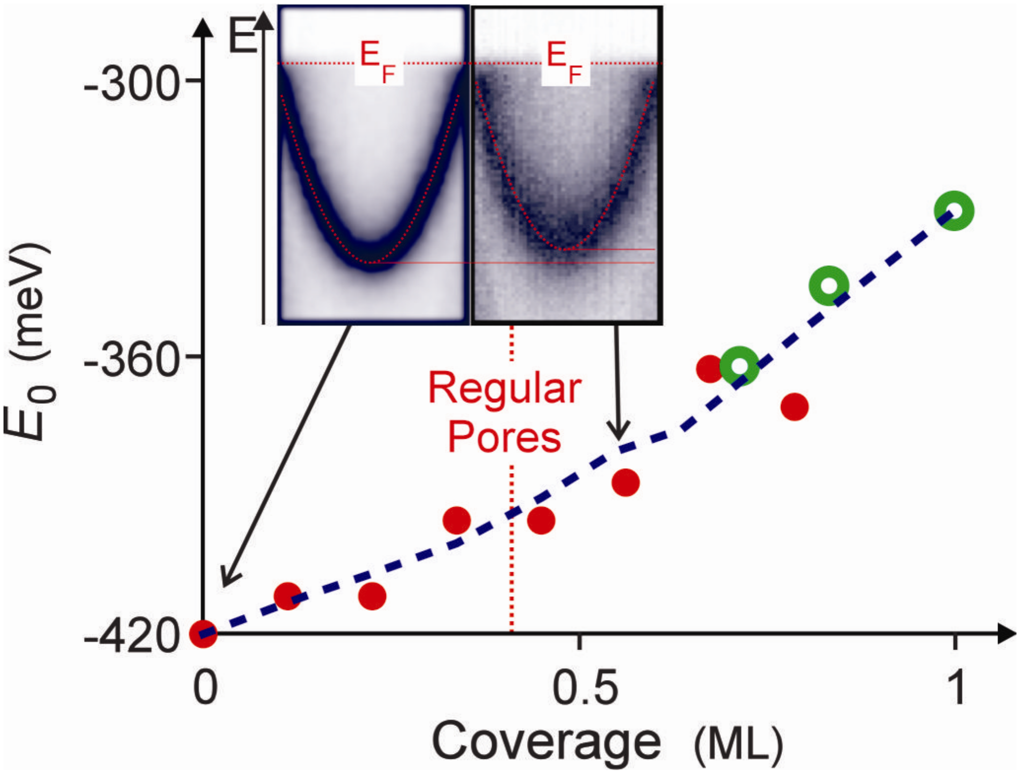

Figure 4.3 ARUPS measured coverage dependence of the surface state band bottom E_0 (red solid dots) and vdW-DF2 calculated coverage dependence of the surface state minimum (green hollow dots). A 5-point average line is included to guide the eye. The inset shows the ARUPS spectra for the clean surface and for the coverage 0.56 ML, with 1 ML being the close-packed coverage and the vertical dotted line marking the coverage of the regular giant honeycomb network (Fig. 1a). With increasing coverage the surface state band shifts up and loses spectral weight.

state and hence, γ, which becomes coverage/pore dependent. In this treatment we assume effects on *m* to be too small to be significant, supported by our theoretical modeling. As a consequence of the shift of E_0, figure 4.2(a) needs to be rescaled, resulting in figure 4.2(b). Remarkably, the electron deficit *Δn* now vanishes for *one pore only*: the one observed experimentally, i.e. a regular hexagon with three molecules per side. This invites the question: Why is this pore different from all other pores?

4.5 Discussion

To answer this question, we turn to the properties of 2D quantum dots: in 1928 Fock solved the Schrödinger equation for a 2D quantum dot with non-interacting electrons confined by a quadratic potential, resulting in successive shells that can accommodate 2, 4, 6, 8, … electrons (including 2-fold spin degeneracy).[88] Subsequently, it has been realized that this results in quantum dots with exceptional stability for magic-numbers N = 2, 6, 12, 20, … of electrons in filled-shell configurations (the equivalent of noble gases).[89, 90] The lowest "orbital" corresponds to an orthogonal pair of simple harmonic oscillators (SHOs) both in the ground state $n_1=n_2=0$, while the second orbital is doubly degenerate, with one SHO in n=0 and the other in the first excited state n=1; the third has either $n_1=n_2=1$ or $n_{1,2}=2$ and $n_{2,1}=0$, etc. (Here we follow Fock's characterization in terms of two SHO quantum numbers $n_{1,2}$ [88] rather than a principal and an orbital quantum number as in Darwin[91] and Kouwenhoven et al. [89, 90])

Fig. 4.4 shows on the left ordinate the spectrum of the regular AQ pores and for the smallest regular pore the ground state and for all other regular pores the 'valence' shell orbital distribution. The states are not perfectly degenerate, as this would require fourfold or circular symmetry, which is not achievable with the 0° or ±120° angles between adjacent molecules in the pore walls. Here the 'valence' shell is the highest energy shell that is (at least partially) occupied to accommodate the number of surface state electrons originally present within the pore area. The local density of states of the orbitals of the experimentally-observed pore has been confirmed by titration through CO adsorption, as recounted in Refs. [5, 6].

We calculate the total energies, relative to E_0, of the electron distribution of each pore when filled up to a closed-shell noble-gas-like configuration and display them as dots referenced to the energy scale on the right ordinate of figure 4.4. Remarkably, regular hexagons always have closed shells and have configurations at or near the lowest energy for each filled shell. Moreover, the experimentally observed pore geometry leads to the lowest overall energy of a closed shell (figure 4.4). Thus, in summary, regular AQ pores on Cu(111) match the size that

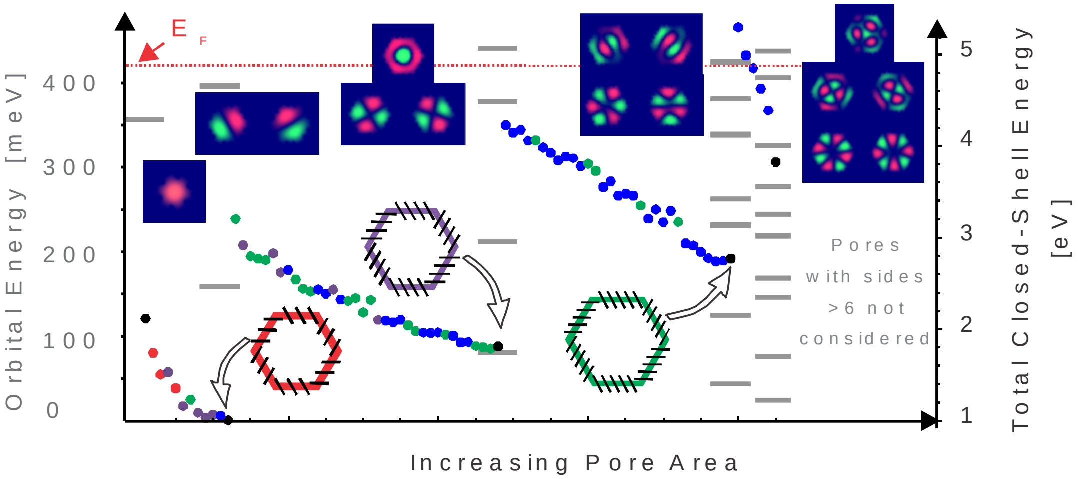

Figure 4.4 Electronic states (grey horizontal bars) of ideal hexagons with 2-6 AQs per side (left y-axis, relative to E_0) and (for 2 AQ) their ground state and (for 3-6 AQ) their 'valence' shell orbitals (i.e. 1st-4th shell). The supporting material lists the spectra of all (not only the ideal hexagons) pores and all electronic states. The y-axis on the right indicates the total electron energy, again referenced to E_0, required to fill all orbitals up to the 'valence' shell for each of the possible AQ pores (same sequence and colors as in Fig. 2a,b). Notably, the experimentally observed one has the lowest energy.

leads to closed-shell 2D quantum dots, with nature choosing the pore that corresponds to the lowest energy closed-shell quantum dot. The dots are sufficiently large that two shells are filled, making the quasi-atom picture more compelling than in previous studies of laterally confined orbitals involving single orbitals.

Our evaluation uses no adjustable parameters and is robust with respect to small variations of the precise location of the surface state scattering and the shape of the E_0 fit curve (linear, square, 5-point average). What we observe amounts to surface-state-driven formation of self-tailored quantum corrals. While the stabilization is not so large as to enable the formation of isolated pores in sparsely covered regions (where, instead, molecular rows form), it does provide an explanation for the surprising regularity of the cells given the high entropy associated with honeycomb cells in most physisorption systems.[92]

Since we could not directly observe these states in ARUPS, we provide an indirect corroboration that the pore size/shape and associated spectrum control the AQ self-assembly into a regular porous network: to this end, we sought and discovered a different adsorbate PQ with closely related substrate interactions (so that the E_0 vs. coverage curve of figure 4.3 is still valid) that assemble into pores with the same size/shape/spectrum as AQ although requiring a different lattice periodicity.

Deposition of PQ leads to a porous network on Cu(111) that does not quite exhibit the perfect ordering of AQ but which prominently features pores of virtually identical size and shape as AQ (figure 4.1(d-f)). Given the larger size and higher aspect of the molecule, the vertex geometry is different from that of AQ and the overall periodicity of the PQ network is substantially larger (see superposition in figure 4.1(f)). Due to the larger molecule body, PQ molecules are found to interact with one another in a larger variety of configurations leading to a far larger range of potential pore configurations. Evaluating PQ networks in the same manner as for AQ, we find that all pores have an electron deficit in the absence of the surface state band bottom shift (figure 4.2(c)). However assuming the same coverage-E_0 shift relationship as for AQ (with 1ML coverage being a smaller number density of molecules for PQ than AQ due to its larger size), we find that the pores of figure 4.1(d,e) stand out as having no electron deficit (along with two others, that do not tile and have a higher closed-shell energy). While the effect is not quite so striking for PQ as for AQ, it does corroborate the singular role of the pore shape/area adopted by AQ and its ability to drive network formation.

Our picture leads to a variety of predictions: if the network is indeed formed through coalescence of the surface state into quantum dots, then modifications of its properties using alkalis and halogens, and (as Fock points out for the 2D SHO[88]) a magnetic field may pose an avenue to varying the surface pattern. Our description in terms of isolated 2D orbitals in each pore is the simplest possible; our DFT calculations suggest that in reality, some coupling between the pores, as envisioned by Lobo-Checa et al.[77] for smaller pores and narrower "walls", is likely to occur and should help stabilize the regularity of the giant honeycomb network. Readers familiar with semiconducting quantum dots may be concerned with the Coulomb repulsion between electrons in the pores, which scales with the reciprocal of the capacitance. On a metal surface, however, screening makes the capacitance enormous and the associated splitting negligible.

4.6 Conclusion

In conclusion, we have found that the surface state cannot only be captured in quantum corrals, but that the surface state itself can also be the driving force behind the formation of corrals that are minutely tailored to optimize the quantum dot character of its electronic setup, leading to coral shapes that are uniform across different adsorbate periodicities. Thus, what started as a survey of their aesthetics finally was realized to be a tool for surface patterning.

Chapter 5

Anthraquinone Network – Part 2

Adsorbates in a Box: Titration of Substrate Electronic States

5.1 Abstract

Nanoscale confinement of adsorbed CO molecules in an anthraquinone network on Cu(111) with a pore size of ≈4 nm arranges the CO molecules in a shell structure that coincides with the distribution of substrate confined electronic states. Molecules occupy the states approximately in the sequence of rising electron energy. Despite the 6-fold symmetry of the pore boundary itself, the adsorbate distribution adopts the 3-fold symmetry of the network-substrate system, highlighting the importance of the substrate even for such quasi-free electron systems.

5.2 Introduction

Understanding the adsorption of molecular species at solid surfaces resonates as one of the unifying themes throughout the evolution of surface science over the past half-century. The adsorption of an ever increasing number of molecules on crystallographic surfaces, as well as on steps and at other defect sites, has been studied. Great progress has been made in the development of computational techniques that reveal the electronic interaction between adsorbates and the underlying substrate atoms. However, the effect of lateral confinement of the support on the nanometer scale has remained largely unaddressed because of challenges in the preparation of surfaces covered with atomically identical patterns several nanometers in scale and because of computational limitations in simulating systems consisting of many hundreds of substrate and adsorbate atoms. Yet many of the applications of surface science, for instance in heterogeneous catalysis or in semiconductor processing, crucially rely on nanoscale-delimited surfaces; and recent progress in these fields emphasizes the effects of nanoscale confinement[93] and diminishing scale, respectively.

In this work we address how confinement of the substrate to approximately 4 nm hexagons, i.e. larger than most adsorbate patterns[77, 94, 95] and substrate unit cells but smaller than previously investigated structures such as quantum corrals and adislands,[62, 96] affects the distribution and energetics of small molecule adsorption. A number of molecular surface networks, such as hydrogen bonded [97] and boron-nitride based[95, 98], have been shown to template adsorption of subsequent species.

It has been shown that perturbation of substrate electronic states, such as an underlying gas bubble[99] or scattering of a Shockley surface state at a step edge[47]or adatom row[100], affect adsorbate distribution. Substrate-mediated long range interactions between molecules have been found in a variety of systems and quantified in a number of cases by scanning tunneling microscopy (STM)[1, 42, 43, 50-54, 66-69] and field ion microscopy.[74, 75, 101] A correlation between the location of CO molecules on Ag(111)[48] and benzene on Cu(111)[47] with the phases of the surface scattering amplitude have been proposed from experimental data and through theoretical modeling.[102, 103] In this experimental study we show that confined electronic states of the substrate can actually be titrated with adsorbates, arguably much as electronic states are filled up from the lowest to highest energy in an atomic orbital diagram.

5.3 Methods

Our measurements were conducted on a Cu(111) surface decorated with a chiral anthraquinone (AQ) network of sixfold symmetry (disregarding the substrate) exhibiting pores that expose 186 substrate atoms in their midst.[1] (figure 5.1(a)) We use CO as our test molecule because a wealth of data on its surface behavior is available: CO molecules adsorb upright atop Cu(111) substrate atoms. They are imaged in STM as protrusions or indentations, depending on whether the STM tip is decorated with a CO atom at its apex or not, respectively.[23]

Sample preparation involves the usual sequence of sputtering and annealing, followed by cooling to liquid nitrogen temperatures. The AQ pattern is created by evaporation of the molecule onto the cryogenic sample followed by annealing to room temperature. Deposition of

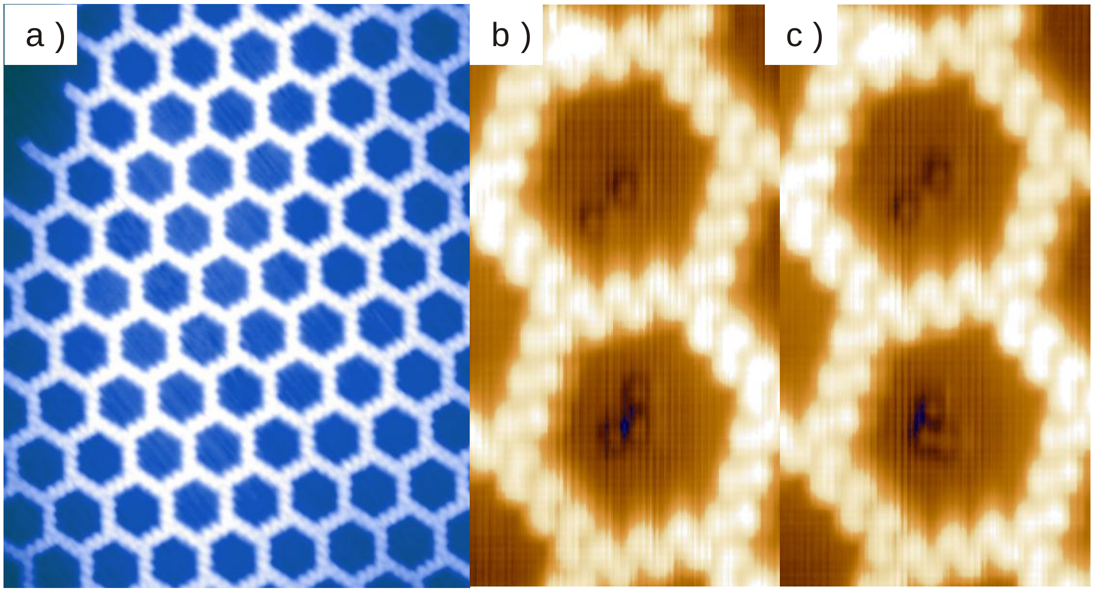

Figure 5.1 (a) array of atomically defined pores on Cu(111) formed by deposition of anthraquinone. Image parameters: 38 nm x 43 nm; Bias: -2.534V; Current: 50 pA **(b,c)** images from a movie showing the diffusion of two and three CO molecules in confinement. Image parameters: 6 nm x 10 nm; Bias: -2.673 V; Current: 99 pA.

CO molecules through a leak valve onto the AQ-patterned surface at 40K preserves the pore shapes.

5.4 Results and Analysis

We find that the AQ network blocks the diffusion of adsorbed CO molecules on the substrate; repeated imaging of the same set of pores allows tracking of the perambulation of a fixed number of molecular entities within a confined area. Figures 5.1(b) and 5.1(c) show images from a series of STM scans of a set of pores, in each of which a few molecules are seen to diffuse. In such sequences of images each molecule can be assigned to a particular substrate atom on which it is adsorbed. From thousands of images obtained, we calculate histograms of the occupation of the various substrate sites within the confined area (figure 5.2(a-e)). Each confined area consists of 62 threefold degenerate (186 in total) adsites surrounding a hollow site at the pore center in a threefold symmetric arrangement. The AQ network is chiral, removing inversion symmetry.

The radial distribution of CO molecules in pores of different coverages is shown in figure 5.3(a). Given the large number of different adsites, we construct 7 radial bins, as indicated in the inset of figure 5.3(a). In pores containing a single CO molecule, the CO is generally found at

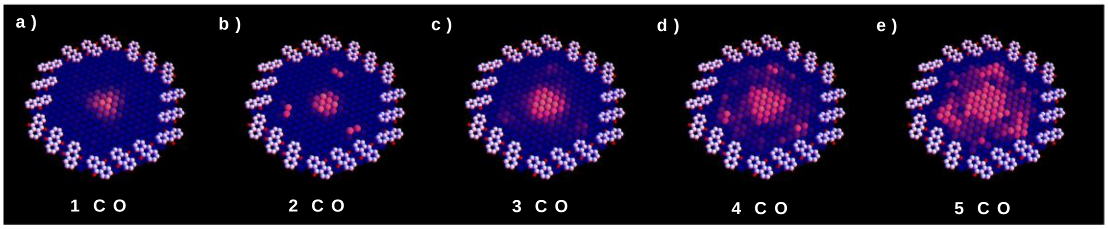

Figure 5.2 Color coded plots of the probability of CO molecule occupation for each of the 186 Cu substrate atoms exposed within an anthraquinone pore. Each plot is based on > 500 CO configurations observed and averaged over equivalent locations.

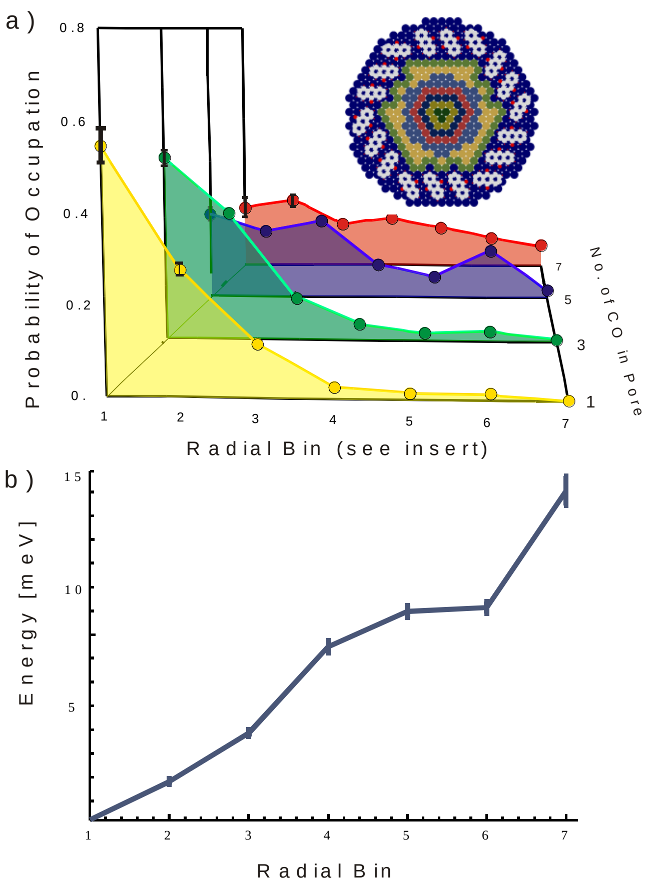

Figure 5.3 (a) normalized probability of occupation of radial bins (shown in the inset, normalized to the number of substrate sites they encompass) for pores containing 1-7 molecules. For 1,3 molecules the distribution is monotonic, whereas at increasing number of molecules also an additional intermediate distance becomes favored until further increase of the coverage renders the plot featureless. **(b)** Variation of the adsorption energy of a single CO molecule across a pore. Error bars are based on √counts in the histogram and are shown in panels **(a,b)** when larger than the data markers.

the pore center; in 54% of the cases, the molecule occupies one of the two inner bins of figure 5.3(a). From the distribution of figure 5.2(a) we can obtain the radial variation of the probability P_i of CO occupation of an adsite *i* indicated in the yellow (front) curve of figure 5.3(a). From this dataset we can construct the canonical partition function Z of the single CO system, which allows us to deduce the radial variation of the CO adsorption energy ε (figure 5.3(b)):

$$Z = \sum_i e^{-\varepsilon_i/k_B T} \quad \text{with} \quad P_i = \frac{e^{-\varepsilon_i/k_B T}}{Z},$$

with k_B the Boltzmann constant and T the temperature 27 K of our measurements. The resultant variation of ≈ 14 meV is quite substantial, approximately 1/5 of the CO/Cu(111) diffusion barrier of 75 meV.[43]

For two CO molecules in the system (figure 5.2(b)), we find generally that either both molecules occupy the confinement center or they are split between the center sites and a set of three equivalent adsites approximately half-way towards one set of confinement vertices. The same set of three adsites is also favored in pores that contain 3-5 molecules (figure 5.2(c-e)). Experimentally, these are independent datasets acquired on different pores, days and sample preparations; the reappearance of the same location for pores of different coverage rules out experimental error (e.g. through subsurface defects) as the origin of the peripheral peaks in figure 5.2. This poses the question of their physical origin and, in particular the reason for their threefold symmetry. The ≈ 4nm diameter of the pore rules out direct intermolecular interactions, suggesting that a substrate-mediated effect may be of relevance. Unfortunately, first-principles computational methods (such as density functional theory) are incapable of treating a system that requires at least 186 substrate atoms per layer (i.e. several hundred in total).

Prompted by the idea that surface states get reconstituted in laterally confined geometries, we turn here to a much simpler continuum model of the surface bound states derived from the Cu(111) surface state. In this context it is important to realize that although the pore boundary itself is sixfold symmetric, the pore vertices are alternatingly centered on hcp and fcc hollow sites, so that the overall symmetry of the pore on the substrate has the same threefold (and not sixfold) symmetry of the CO distribution.

Thus, we calculate the confined electronic states within the pore starting from the known solutions of a particle in a triangular box[104], followed by relaxation into the actual geometry of the pore. Gross et al. showed that scattering of the surface state from organic molecules occurs not at the peripheral hydrogen atoms but at the 2nd period elements.[78] Hence, we construct the boundary of our pore from the six carbon and oxygen atoms per molecule (102 in total) that are closest to the pore center. We adapt an iterative finite-difference algorithm[105], more commonly used for solution of Poisson or heat-diffusion equations, to the relaxation of the known solutions into the geometry of the pore. Here, we develop the wave function in a Taylor series to third order, summing over four locations adjacent to a point (x,y) to reproduce the Hamiltonian H_{inside} inside the potential- free pore:

$$\frac{\langle x+\delta,y| + \langle x-\delta,y| + \langle x,y+\delta| + \langle x,y-\delta|}{\delta^2}|\varphi\rangle - \frac{4\langle x,y|\varphi\rangle}{\delta^2} \cong \left\langle x,y\middle|\left(-\frac{2m^*}{\hbar^2}\right)\hat{H}_{inside}\middle|\varphi\right\rangle$$

$$= \left\langle x,y\middle|\left(-\frac{2m^*}{\hbar^2}\right)E\middle|\varphi\right\rangle,$$

with m^* the effective mass of an electron of the surface state of 0.34 electron masses and δ a small displacement. Thus, if φ_{n-1} is an approximate eigenfunction of the Hamiltonian, a better approximation φ_n can be found by evaluating

$$\langle x,y|\varphi_n\rangle = \frac{\langle x+\delta,y| + \langle x-\delta,y| + \langle x,y+\delta| + \langle x,y-\delta|}{4 - 2m^*\,\delta^2\,E_{n-1}/\hbar^2}|\varphi_{n-1}\rangle\,.$$

Alternating this iteration and Gram-Schmidt orthogonalization[106] of the set of eigenfunctions originally obtained from the triangular particle in the box problem, we end up with three eigenfunctions (one unique and one twofold degenerate) whose eigenvalues E of 170 meV and 440 meV, respectively, are below the Fermi Energy E_F, if measured from the bottom of the surface state band of 450 meV below E_F.[85, 86] Figures 5.4(a) and 5.4(b) show the

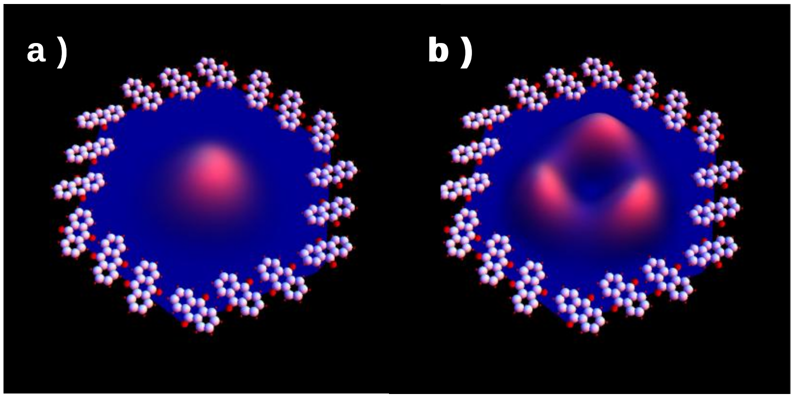

Figure 5.4 Plots of the local density of states of **(a)** the lowest-energy electronic state of the pore and **(b)** superposition of the two degenerate second electronic states of the pore. Compare to the distribution of molecules in pores in figure 5.2.

distribution local density of state (DOS) associated with the first and twofold-degenerate second state, respectively. Our algorithm provides correct eigenfunctions that are converged and invariant to the grid spacing δ of 1.25 Å, 0.63 Å, or 0.41 Å (corresponding to using a 40x40, 80x80 or 120x120 points grid to represent the pore); however, it cannot guarantee completeness of the set of eigenfunctions and eigenvalues found. Summation of the fraction of the surface Brillouin zone filled by the surface state (characterized by the Fermi vector k_F = 0.21 Å^{-1})[86, 107] over the exposed substrate atoms leads to no more than 3 complete electron pairs in the surface state within each pore, in good agreement with the three states found. This result is further corroborated by the recent finding of Lobo-Checa et al. by electron spectroscopy that in a molecular surface network of roughly 1/3 the size of our system there is exactly one confined state.[77]

5.5 Discussion

Comparison between the DOS of figure 5.4 and the molecular distribution within the pore of figure 5.2 shows that CO molecules preferentially occupy locations in the pore that feature a high DOS of the confined surface state, supporting a picture that adsorption energy increases with DOS (and that CO-CO repulsion is relatively insignificant). Moreover, we find that if only one molecule occupies the pore, it seeks out preferentially the pore center where the lowest- energy confined surface state is located. Increasing the coverage leads to occupation of locations corresponding to the more energetic second confined state. Thus, increase of the CO coverage may be likened to the 'titration' of the locations inside the pore that show appreciable local density of states of the confined surface state. The fact that the sequence in which these locations are occupied matches the energetic succession of the corresponding confined surfaces states reminds one of the filling of electrons into an atomic orbital diagram.

Previous modeling of surface-state-mediated interaction of adsorbates has generally employed a scattering-based formalism related to the modeling of the lateral surface state distribution at E_F visible in STM. This has been shown to work well for systems that involve no confinement of the surface and/or dimensions much longer than the surface state Fermi wavelength.[66, 102] The energy integrated approach described here is more suitable to the relatively small scale of pores in molecular surface networks where the confinement size does not exceed the Fermi wavelength by much. Fiete and Heller showed for circular quantum corrals that at larger corral size both approaches lead to equivalent results for the surface state local density of states.[85]

Increasing the number of molecules inside the pore beyond the number of electrons in the surface state (i.e. 6) causes the radial distribution of molecules in the pore to become more uniform (red curve in figure 5.3(a)), showing the limitation in adsorbate guidance achievable in a pore of given size. This finding corresponds with CO's ability to quench the surface state at relatively low coverage.

5.6 Conclusion

Although our calculations were based on free-electron-like behavior of the surface state electrons (i.e. a constant potential within the pore boundary) with just an effective mass accounting for the presence of the substrate, our finding of threefold symmetry (as enforced by the substrate, in contrast to the sixfold symmetry of the molecular network) is crucial for explaining the experimental distribution of adsorbates; this highlights the limitation of the free electron approximation in understanding surface state electrons and their impact on adsorption. In summary, by monitoring adsorbate diffusion within a nanometer-scale confined system we found that such confinement has a pronounced effect on their average location, suggesting that engineering of confinement boundaries may not only allow engineering of surface electronic states but can also be a tool in assembling molecular patterns at surfaces.

Chapter 6

Anthraquinone Network – Part 3

The Power of Confinement: Adsorbate Dynamics on Nanometer-Scale Exposed Facets

Reprinted with permission from [6]. Copyright (2010) American Chemical Society.

6.1 Abstract

The diffusion and arrangements of CO adsorbates within nanometer-scale pores on a copper surface are investigated by low temperature scanning tunneling microscopy. In contrast to extended terraces, confinement stabilizes dislocation lines that expose > ¼ of the adsorbate population to potentially more reactive adsorption configurations. Confinement allows correlation between adsorbate diffusivity and the number of adsorbates in the pore. A marked increase is found which coincides with the absence of dense films on the exposed facets. In combination, we find that in confinement CO molecules are much more likely to be at adsorption sites that allow lateral access, in contrast to the dense and uniform films on extended terraces.

6.2 Introduction

Nanoscopic metal facets have considerable technological relevance, for instance on supported metal catalysts for applications ranging from the (petro-)chemical industry to emission control, yet the diffusive behavior of adsorbates has so far generally been studied on extended terraces, i.e. not under lateral confinement, mainly due to experimental obstacles. For the study of the dynamics of adsorbates on nanoscale clusters, it would be ideal if arrays of atomically identical ones could be formed. Absent this possibility we utilize a Cu(111) substrate covered with a self-assembled anthraquinone network (figure 6.1(a)). This network sustains subsequent deposition of CO molecules and confines their diffusion into pores of ≈ 4nm in size, where it can be imaged and studied in detail.

The pores have a similar size as the facets expected on catalytic nanoclusters; in particular, studies on gold have shown that its activity increases enormously if dispersed in this

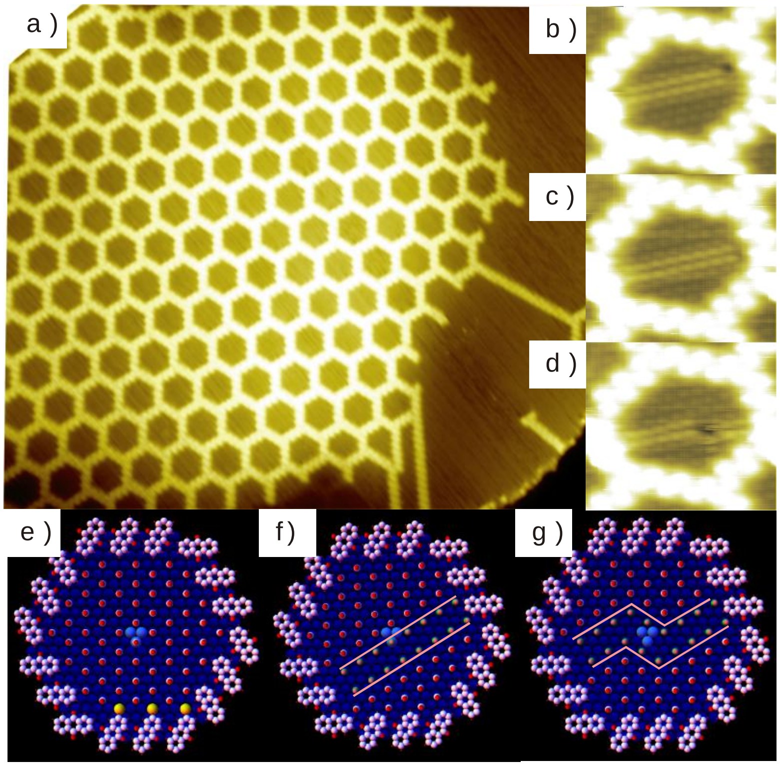

Figure 6.1 (a) array of atomically defined pores on Cu(111) formed by deposition of anthraquinone according to Ref. [1] Image parameters: 83 nm x73 nm; Bias: -2.53V; Current: 50 pA, Temperature 90 K; **(b,c,d)** images from a supporting movie of a dislocation line moving in confinement. Image parameters: Bias -2.40 V, Current 44 pA, Temperature: 24 K **(e,f)** The (√3x√3)R30° adlayer can be anchored at any one of the three atoms at the center of the exposed facet (light blue). In each case, one facet edge is decorated differently than the remaining two of the same kind (yellow in **(e)**). This can be alleviated, if a dislocation line is induced in the pore **(f)**. In both cases the same number of molecules fit inside the pore. **(g)** Model of a kink in a dislocation line similar to the STM image of panel **(d)**.

size regime.[108, 109] Conventionally, the high activity of nanoparticles, as compared to the surfaces of bulk metals, is attributed partly to the high surface to volume ratio at high dispersion, and partly to support-metal interactions and the abundance of surface defect sites such as step-/facet-edges and -kinks.[110] While the exposed copper facets of our network probably have little besides their size in common with catalytic nanoparticles, they nevertheless open for study the kind of effects that lateral confinement may have on the dynamics of adsorbates, at least in a phenomenological manner; a survey of them is the objective of this study.

Several previous publications addressed the dynamics of adsorbates at metal surfaces and their interaction with one another. They include measurements of the dynamics of benzene molecules,[111, 112] reactive mixtures,[113, 114] hydrogen atoms,[115] and CO molecules.[42, 43, 48, 116-118] Also, the insertion of atoms or molecules into molecular surface networks has been studied previously.[94, 97, 98, 119-121] What makes our study novel is the confined nature of the adsorbates that allows us to study how molecules behave when their support is not a large, clean and inert terrace.[122]

We use CO as our test molecule because abundant data on its surface behavior is available: CO molecules adsorb upright atop Cu(111) substrate atoms. They are imaged in scanning tunneling microscopy (STM) as protrusions or indentations, depending on whether the STM tip is decorated with a CO atom at its apex or not, respectively.[23] At sufficient coverage, CO adsorbates form an ordered (√3x√3)R30° overlayer; large islands of this superstructure have been observed in previous STM studies.[123] In our model system there are 186 exposed atop adsites in each 4 nm pore, allowing a maximum occupation in the exposed facet of 62 CO molecules in a dense (√3x√3)R30° adlayer.

6.3 Methods

Initial sample preparation involves the usual sequence of sputtering and annealing, followed by cooling to liquid nitrogen temperatures. The anthraquinone pattern is created by deposition of the molecule onto the cryogenic sample followed by annealing to room temperature. After subsequent cooling to ≈ 40 K, CO is deposited through a leak valve.

6.4 Results and Analysis

Deposition of CO molecules into an anthraquinone honeycomb network does not alter the pore shape. With careful dosage we obtain a CO coverage very close to a complete (√3x√3)R30° overlayer, which is visible inside the pores (figure 6.1(b-d)). Moreover, we find on the exposed facets a dislocation line which is constantly present yet persistently shifting position. This differs from the behavior of CO films on extended terraces, where the (√3x√3)R30° is observed over large areas and dislocation lines (i.e. antiphase domain boundaries) are expelled to the edge.[123] What is the origin of this effect?

Each exposed facet is centered around a substrate hollow site, allowing three equivalent atop adsites (light blue in figure 6.1(e)) to anchor the CO (√3x√3)R30° pattern, thus spanning three equivalent overlayer sublattices. The facet edges consist of two alternating sets of three equivalent sides, much as any hexagonal fcc island is surrounded by steps with alternating (111) and (100) facets. One of the sets of sides is equally decorated with CO molecules no matter which central substrate atom anchors the overlayer. Of the other set of sides, however, only two are covered intimately, leaving open space near the third side (yellow in figure 6.1(e)).

The open space can be avoided if the CO adlayer is imperfect: a dislocation line in the overlayer allows placement of adsorbates at all sides of the second set equivalently. Consequently, the confined adlayer is under competition between forming the structure found on extended surfaces and incorporation of a dislocation line that permits equal filling of the edge sites, i.e. providing optimal edge interaction at the expense of intermolecular interaction. In both cases, the same number of CO molecules fit onto the exposed facet. The observation of the persistence of the dislocation lines indicates that the interactions at the adlayer edge are dominant over those within the adlayer.

Imaging 75 setups of one dislocation line at 24 K, we find that in ≈ 40% of the cases a kink is present in the line. A dislocation typically affects 16 molecules (8 per side); a kink in the double line increases this number by 2 along the dislocation line (figure 6.1(g)). Analyzing the measured fraction of kinked lines using the Boltzmann equation and taking into account the degeneracy of the various possible kinked configurations, we estimate a kink energy of 6.1 ± 0.3 meV and a total energetic cost of the entire dislocation line of ≈ 0.05 eV. For three molecules the edge-interaction is improved by the dislocation line (yellow in figure 6.1(e)). This yields a lower boundary of the edge interaction of ≈ 0.02 eV per molecule, a considerable energy compared to, e.g., the CO diffusion barrier of 0.075 eV.[43]

The presence of the dislocation can potentially affect the chemical reactivity of the film markedly: molecules affected by a dislocation line have a nearest neighbor configuration that allows more ready access to them as well as the underlying substrate. The number of molecules affected by the dislocation scales linearly with the size of the facet, whereas the total number of molecules scales quadratically, indicating that the smaller the facet size, the more pronounced this effect. For the 4 nm facets studied here, more than ¼ of the adsorbates (16 out of 62) are directly affected by the dislocation line, significantly greater than on extended terraces.

The constant motion of the dislocation lines well below 30 K contrasts substantially with the behavior of individual CO molecules on Cu(111), whose diffusion starts only at ≈ 33K.[43] Is this effect limited to dislocation lines? Preparing films of slightly lower coverage with facets that have a small number of vacancies in their (√3x√3)R30° coverage (figure 6.2(a,b)), we observe rapid motion at similarly low temperature. While increased diffusivity at high coverage has been observed in the past – to our knowledge it has not yet been quantified except at very low concentration[43] and for direct neighbors.[66, 117, 124] The confined nature of our exposed facets allows us to monitor the diffusion rate for a fixed number-density of molecules. The dotted line of figure 6.3 shows the diffusivity from a few molecules per pore (figure 6.2(e,f)) up to the point at which the (√3x√3)R30° adlayer is 1/3 complete and site blocking becomes important (figure 6.2(c,d)). While data points for coverages up to 6 molecules on the exposed facet were measured at 27 K, diffusion at higher coverages was too rapid at this temperature; the data point for 21 molecules per pore was measured at 22 K and scaled according to the

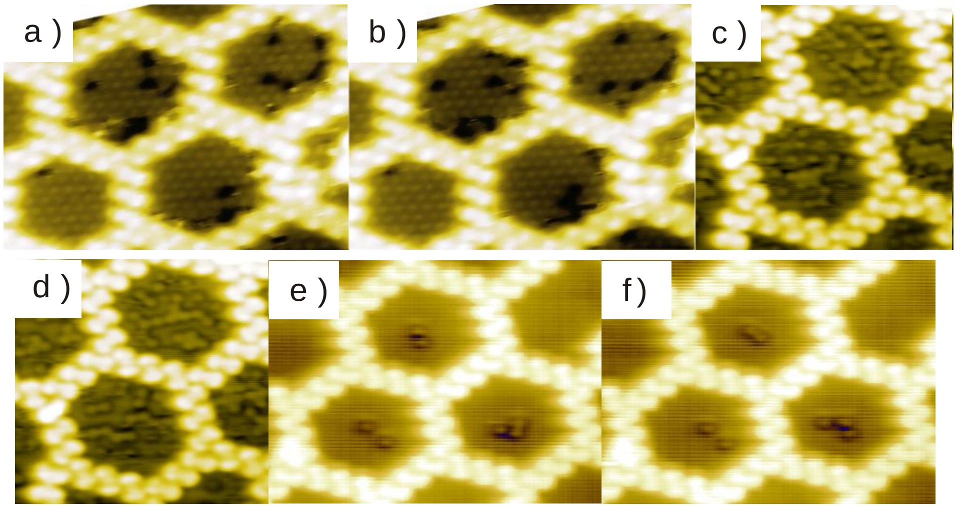

Figure 6.2 images from STM movies showing the diffusion of **(a,b)** vacancies in a (√3x√3)R30° CO coverage in confinement (image parameters: 12 nm x 9 nm; Bias: -1.23 V; Current: 120 pA, Temperature: 23 K); **(c,d)** 20-22 CO molecules on each exposed facet (image parameters: 8 nm x 8 nm; Bias: -0.72 V; Current: 60 pA, Temperature: 22 K); **(e,f)** two and three CO molecules in confinement (image parameters: 12 nm x 9 nm; Bias: -2.67 V; Current: 100 pA, Temperature: 27 K).

Arrhenius parameters of Ref. [43]. The dotted line represents an exponential fit of the diffusivity.

A detailed look at the STM images indicates that the diffusivity depends not only on the number of molecules on the exposed facet but also on the position of the molecules within that facet. Generally, molecules tend to move less if they are closer to the center and more rapidly around the perimeter. Unfortunately, this renders a complete Arrhenius-based evaluation (which would need to separate molecules by location) beyond reasonable effort.

Thermally programmed desorption experiments showed that an increase of the surface coverage can lead to a reduction of the adsorption energy.[110] In the simplest approximation, the diffusion barrier is a constant fraction of the adsorption energy. While this argument justifies a variation of the diffusion barrier with coverage, it provides little indication that the diffusion preexponential factor should vary markedly with it. Fixing the diffusion prefactor at the

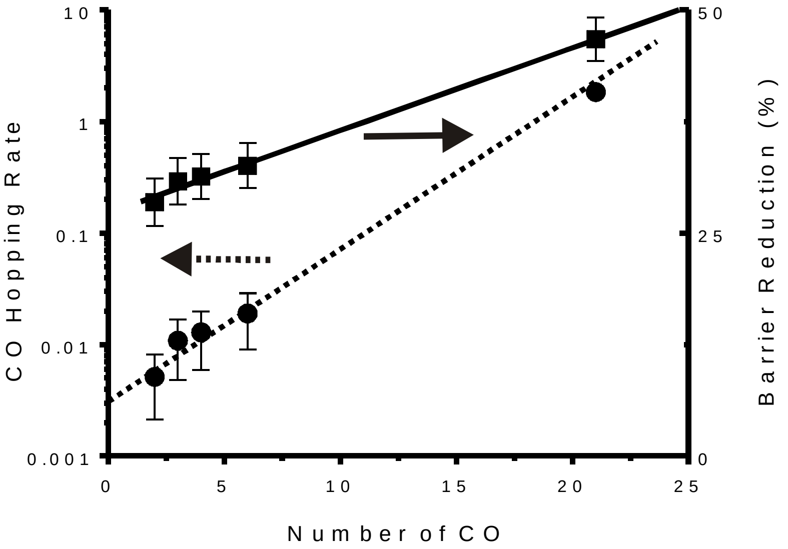

Figure 6.3 dotted line: diffusion rate per molecule as a function of number of molecules on an exposed facet; solid line: reduction of the diffusion barrier that causes this acceleration under the assumption of a constant diffusion prefactor. All error bars are dominated by the temperature uncertainty of 1 K in our measurements; the statistical error is much smaller than the data markers.

value for isolated molecules,[43] the variation of the diffusion barrier with coverage can be obtained from the diffusion data (figure 6.3, solid line). The adsorption and subdivision of the Cu(111) terrace by the anthraquinone network causes a reduction of the CO diffusion barrier by ¼; increasing the coverage inside the pore up to 1/3 of the $(\sqrt{3}x\sqrt{3})R30°$ adlayer reduces the diffusion barrier by another ¼. The data suggests a linear fit of the reduction of the barrier as a function of the coverage with a slope of (57 ± 14) %/ML, with 1 ML defined as the complete $(\sqrt{3}x\sqrt{3})R30°$ coverage. If the adsorption energy is assumed to be proportional to the diffusion barrier, then its reduction by half indicates a comparable reduction of the adsorption energy. The observation of a linear dependence of the energy reduction on the number density of molecules suggests that its origin is not direct pair interactions (which scale quadratically with coverage) but involves the substrate, potentially both through confinement-induced surface state effects[62, 77, 85] or through mediation of trio and higher order interactions.[102] While the effects of site blocking and nearest neighbor interactions prevent us from obtaining experimental data beyond 1/3 ML coverage, our results suggest a quite substantial destabilization of the CO molecules in the $(\sqrt{3}x\sqrt{3})R30°$ adlayer, well in line with the results discussed in Ref. [110, 124]

Following this discussion of the CO dynamics, we finally examine the locations the molecules/vacancies occupy and the effect of the lateral confinement on them. To this end, we study the distribution of vacancies in coverages like the one shown in figure 6.2(a-d) and of molecules in coverages like shown in figure 6.2(c,d).

Figure 6.4(a) shows the likelihood that the dislocation line of Figure 6.1(b,c,d) occupies different substrate sites in a color-coded histogram. In this context it is important to realize that although the anthraquinone network appears sixfold symmetric, due to the threefold (and not sixfold) symmetry of the substrate, every other of its sides comes to rest at different surface locations. The dislocation line generally crosses near the center of the exposed facet thereby connecting dissimilar edges. Consequently, the area showing higher occupation of the dislocation line in the center right of figure 6.4(a) is not equivalent to the area on the center left of the pore line. The sensitivity of the dislocation line to the geometry of the facet boundary is a testament to the importance of confinement for the spatial distribution of adsorbates.

Figure 6.4(b) shows the distribution of vacancies on exposed facets a few molecules short of saturation; bright colors correspond to a high likelihood of finding vacancies. Viewing a large number of movies with coverages similar to figures 6.2(a,b), we qualitatively observe that the vacancies frequently arrange themselves in rows that originate at the facet edge and often

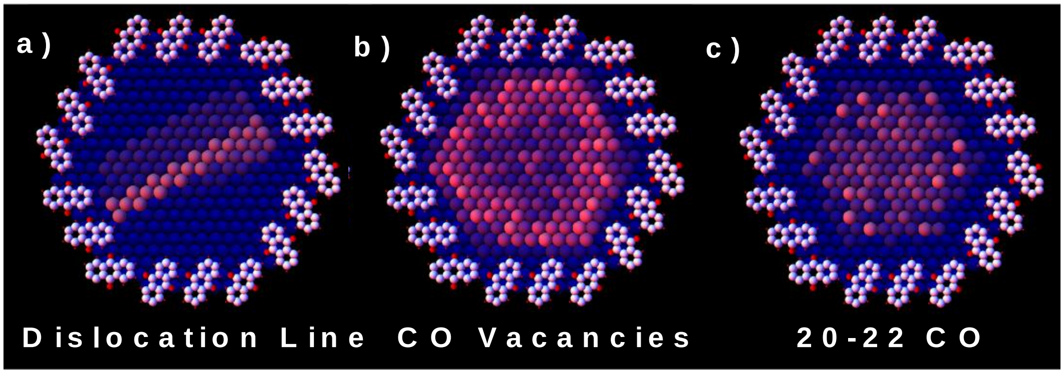

Figure 6.4 color coded histograms of CO vacancy/molecule distribution for each of the 186 Cu substrate atoms exposed within an anthraquinone pore. The anthraquinone pore is chiral and threefold symmetric, panels **(b)** and **(c)** are averaged over three equivalent rotational orientations. **(a)** Dislocation lines are most commonly found to cross the facet center, **(b)** whereas vacancies are more commonly found around the facet edge. **(c)** For 20-22 CO molecules a relatively featureless distribution is observed. Each panel represents the location of >1000 vacancies/molecules.

bend back towards the same or an adjacent edge. In the histogram of figure 6.4(b), this is reflected in a higher probability for vacancies to be found at the edges, with a slight preference for one kind of edge and vertex. It is important to realize that in our observation, the vacancies do not segregate from the adlayer, i.e. they do not form a closely covered area surrounded by empty space as on extended terraces.[123] Rather the vacancies are interspersed with the adlayer, affecting a far greater fraction of the adlayer molecules and potentially rendering the adlayer more reactive. A statistical analysis of vacancy motion is much more complicated than for adsorbate motion, as in the (√3x√3)R30° overlayer 'fractional' vacancies (corresponding to molecules adsorbed in antiphase) can combine and molecules can occasionally and intermittently adsorb closer than the √3 spacing, so that the total number of vacancies on an exposed facet is not conserved.

Reducing the coverage to 20-22 molecules on the exposed facet (i.e. ≈ 1/3 of the (√3x√3)R30° adlayer), we do not observe aggregation into large islands (figure 6.2(c,d)). Despite the low temperature only small aggregates of molecules form, with almost every molecule being accessible on the surface from at least one side. This is, again, in marked contrast to CO films on extended terraces, where we find extended (√3x√3)R30° islands under similar conditions.[123] The distribution of molecules within the exposed facet is relatively featureless; no preferred or avoided regions of adsites can be discerned (figure 6.4(c)).

6.5 Conclusion

In summary, we conducted a survey of the effects that nanometer-scale confinement can have on adsorbate dynamics and placement: on small exposed facets we found that adsorbate diffusion increases rather than decreases, resulting in more even and open distributions of adsorbates and adlayer vacancies than found on extended terraces. Even at full coverage, confinement can stabilize dislocation lines which affect a substantial fraction of the molecules in the adlayer (> ¼ of them). In combination, these findings suggest that confinement alone can increase the potential for surface reactivity in an adsorbate film: the smaller the facet size (i.e. the smaller a metal nanoparticle that creates it), the more pronounced the mentioned effect.

Chapter 7

Molecular Orbital Analysis of Anthracene Derivatives on Cu (111)

7.1 Introduction

Density functional theory (DFT) simulations have become a ubiquitous and indispensible tool in many areas of chemistry. In surface science, their use includes determining the adsorption geometries of a vast array of organic molecules on metal surfaces through geometric optimization based on minimization of the total energy of appropriately chosen super cells comprising both the adsorbate and several substrate layers. This approach has allowed for the understanding of surface pattern formation in a plethora of adsorption systems; likewise, it has permitted simulation of molecular motion at surfaces at great fidelity. The overall success of this method is beyond doubt. Yet from a chemical perspective this approach is somewhat unsatisfactory, as interpretation of its results, i.e. charge density distributions, and their reconciliation with a molecular-orbital approach to chemical understanding is difficult and cumbersome and, hence, all too often not even attempted. Here, we present a facile and very informative way of analyzing DFT data on molecular adsorption at metal surfaces that provides a direct bridge to a more chemical and molecular-orbital oriented understanding of the phenomenon.

We stress that our approach does not generate novel or better data *per se*, but submit that the understanding of the adsorption and diffusion processes it furthers may lead to fundamentally improved insights into surface chemistry, with a potential host of applications. In particular, we demonstrate a way of obtaining a molecular orbital (MO) theory picture - including MO diagrams - by means of utilizing the projections of the Kohn-Sham (KS) orbitals onto the partial waves of each atom that are generated by typical DFT codes using projector augmented waves (PAW). As a consequence, we can highlight the impact that individual functional groups play in the adsorbate-substrate interaction, directly relating DFT-analysis to conventional chemical intuition; in fact, application of KS orbitals to an MO analysis is perfectly reasonable, if not more appropriate than some of the more traditional orbitals (e.g. Hartree-Fock), that are typically applied to a qualitative MO theory picture.[9, 10]

As an example, we apply our method to a family of anthracene derivatives adsorbed on the Cu (111) surface: Anthraquinone (AQ), Dithioanthracene (DTA), and Diselenoanthracene (DSeA), as well as anthracene (A) itself (a fairly rigid linear combination of three fused benzene rings, figure 7.1(a). AQ, DTA, and DSeA are derived from anthracene by replacing the hydrogen atoms at the 9,10-positions with the elements O, S, and Se respectively, which lie in the chalcogen group of the periodic table. Because of the chalcogens' comparatively strong interaction with the substrate, we refer to them as linkers in this work. It should be noted that, while DTA and DSeA typically have extra functional groups attached to their linkers, it is possible to deposit them on the Cu (111) surface and then remove those functional groups by annealing, resulting in all three species having the same basic structure.

This class of organic molecules deposited on Cu (111) is of particular interest because these molecules have shown some promise as molecular machinery: they are able to diffuse uniaxially along the [110] direction in the plane of the Cu surface and, in the case of AQ, even act as a cargo-carrying agent.[81, 125] Both AQ and DTA are also capable of creating long-range ordered structures on the Cu (111) surface (hydrogen bonded chains[71] in the cases of both

DTA and AQ, and a honeycomb network[1] in the case of AQ). Anthracene derivatives in general have also been shown to have applications in photovoltaic devices[126] and electronics[127].

In this work, we first examine the geometric and energetic details of adsorption for each species including unsubstituted anthracene. We then reexamine adsorption from the point of view of the molecules' KS orbitals, which we show can readily be partitioned into contributions from KS states of the anthracene and contributions from KS states derived from the linkers. This permits us to identify which states among these participate in hybridization upon adsorption (i.e. which molecule states are most involved in bonding to the substrate). As a consequence, we can systematically (in a chemical sense) analyze the variations in impact this related set of functionalities has. These are then compared to experimental scanning tunneling microscopy (STM) data on these species, of which the aspects concerning anthracene, AQ and DTA have been published already, but not the data concerning DSeA.

The principle findings of this study are that observed differences in diffusion barriers measured by STM can be linked to differences in how linker-derived states of each species hybridize to the underlying Cu (111) substrate by direct side-by-side comparison of MO diagrams of each adsorbed system. In particular, DSeA is found to bind its chalcogen linkers in a fundamentally different way than its counterparts, suggesting an explanation for a lower STM measured diffusion barrier when compared to AQ and DTA.

7.2 Methods

DFT calculations use the VASP code[27-30] with the optB86b-vdW [128, 129] exchange–correlation functional and a projector-augmented-wave (PAW) basis[33, 34]. The PBE-GGA[31, 32] functional was also used to measure binding energies for comparison. Calculations were performed for each molecule deposited on an 8-layer Cu slab, 6x5 atoms in the lateral dimensions; dipole corrections were employed to cancel the effects of any induced dipoles. All results are optimized so that the remaining forces are less than 0.03 eV/Å. Because of the large size of the unit cell and the ensuing small volume of the first Brillouin zone, we sample k-space exclusively at the gamma point. Plane wave and augmentation charge energy cutoffs of 400 and 700 eV, respectively, were used. A detailed explanation of the MO analysis methods performed is presented later, in section 7.4.

7.3 Results: Adsorption Energies / Geometries

Before developing a systematic molecular orbital picture of the variations of the

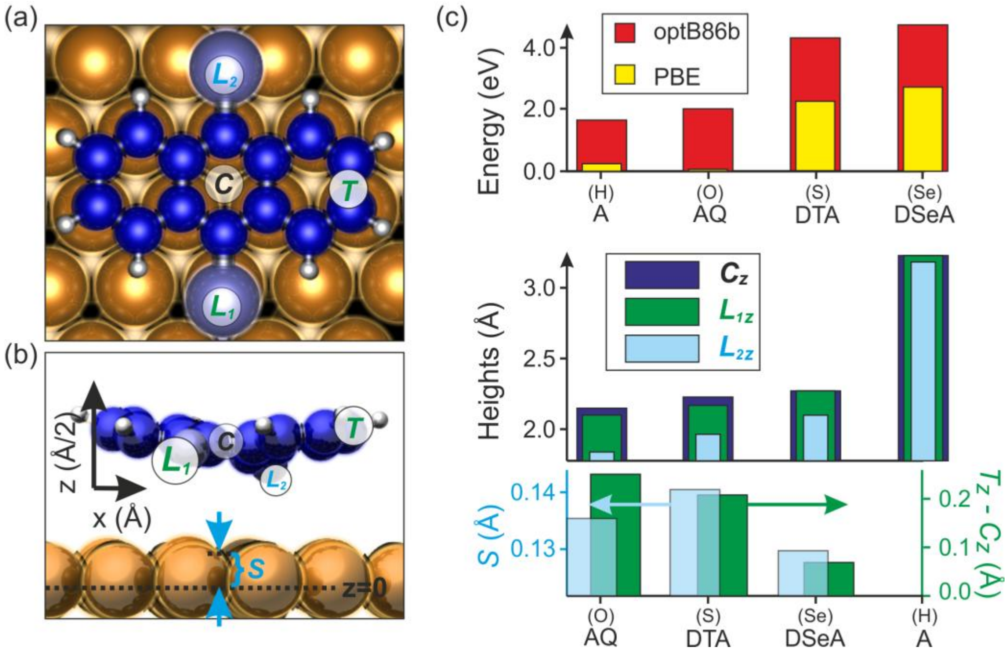

Figure 7.1 Geometric and energetic properties of adsorbed anthracene and its derivatives. **(a)** Top-view of a generic anthracene derivative in its optimum adsorption configuration, with center, *C*, positioned above an hcp hollow, and designation of positions (indicated as circled letters): linkers L_1, L_2, and the terminal edge, *T*, of the anthracene moiety. **(b)** Angled side-view with vertical *z* scale doubled to highlight vertical displacements, illustrating the same positions as **(a)** as well as the displacement *S* of the furthest displaced Cu surface atom. **(c)** From top to bottom: binding energies of anthracene and its derivatives, z-coordinates of the positions illustrated in **(a,b)** for each species (with the same ordering as the graph below), and measured distortions of the substrate (left axis) and molecule (right axis).

substrate-linker-backbone or adsorbate-substrate interactions in each adsorption system, we first describe the overall adsorption geometry and associated binding energies. Figure 7.1(a,b) shows top and side views respectively of what we consider to be the minimum energy adsorption configuration taken by anthracene derivatives on the Cu (111) surface. One linker lies at an atop site while the other lies at or near an fcc hollow site; the rings of the anthracene backbone are centered above hcp hollows. This determination was made by noting that the long axis of the anthracene backbone points along the close-packed [110] direction in STM images,[81, 125] and choosing the minimum relaxed configuration as determined by DFT that yields a long axis pointing in that direction.

The binding energy graph of figure 7.1(c) shows that each anthracene-derived molecule is stable on the surface with binding energies increasing as the linker species proceeds down the periodic table from H to Se. The need and utility of incorporation of a vdW-DF functional is expected from [130]. Calculations without the vdW-DF corrections (PBE-GGA) yield low binding energies for AQ on the order of a few hundred meV which is not consistent with experiment in which AQ sticks on Cu(111) up to room temperature [1] and beyond. This is in line with other non-vdW DFT studies of aromatic systems on metal surfaces in which calculated binding energies are found to be underestimated when compared to experimentally determined binding energies and have been linked to a lack of proper accounting of the van der Waals forces.[131]

Further light is shed on the trend in binding energies when the geometries of the molecule and substrate upon adsorption are taken into consideration (since PBE-GGA has difficulty binding AQ we present only the results for the optB86b-vdW functional here; we also find essentially similar results using the optB88-vdW functional). The linker atoms of each anthracene derivative are pulled close to the substrate (compare the linker z-coordinates L_{1z} and

L_{2z} to the central ring heights C_z of each molecule in figure 7.1(c)) while the anthracene backbone bends upward in a v-shape as can be seen in the side view of figure 7.1(b) in which the direction normal to the Cu surface, z, has been exaggerated for clarity. From the values of C_z shown in figure 7.1(c) it can be seen that anthracene comes to rest more than 3 Å above the surface. This explains why, when the linkers force the central ring to be pulled closer to the substrate, the ends of the anthracene backbone try to pull away, creating a v-shaped molecule which appears as a set of 2 lobes in STM images.[1, 125] The relative degree of bending for each molecule is indicated by the height of the terminal carbon atoms (marked as T in figure 7.1(a,b)) above the central ring, with that of unmodified anthracene being zero (i.e. the anthracene is flat) in agreement with experiment [132]. The general trend of increasing central ring height follows that of the increasing linker atomic radius from O to Se. It may also help to explain the same trend in binding energy: forcing the anthracene backbone closer to the substrate is less energetically favorable, which can also be seen in the trend of decreasing $T_z - C_z$ (bottom right axis of figure 7.1(c)). The substrate distortion, measured here as the z-coordinate of the most uplifted Cu atom, also appears to mirror this trend of decreasing interaction for AQ and DSeA, though DTA shows more substrate distortion than AQ.

7.4 MO Diagram Implementation

In order to evaluate the different impacts of the chalcogen linkers, we need to identify which electronic states appear when they are substituted and how these states shift in energy and real space, as the linkers are varied. To this end, we take the KS states of each system and create the site projected overlap integrals between pairs of states (one from each system): if the squared magnitudes of their projections onto one another are above a threshold within the PAW spheres of the atoms that remain the same upon substitution, then they are considered to be the same state, or at the very least can be considered to be derived from one another. Here, PAW spheres refer to the regions surrounding each atom over which the projectors are defined (those regions where electronic wave-functions would typically oscillate rapidly).

As an example, if we wish to relate unsubstituted A to AQ, we perform DFT calculations on the two related systems: A isolated in vacuum, and AQ isolated in vacuum. Then, since the hydrogen and carbon atoms of A remain unaltered in the substitution that yields AQ, (with the exception of the 9,10 hydrogens which are replaced by O atoms), the projection of the state $\langle\psi_m^A|$ from A onto the state $|\psi_n^{AQ}\rangle$ from AQ is given by:

$$\langle\psi_m^A|\psi_n^{AQ}\rangle = \sum_a \sum_i \langle\psi_m^A|\tilde{p}_i^a\rangle\langle\tilde{p}_i^a|\psi_m^{AQ}\rangle\,, \qquad \text{(EQ 7.1)}$$

where the first sum is over the atoms, *a*, that remain unchanged (in this example the carbon and hydrogen atoms), the second sum is over the partial wave indices, i, centered at each of these atoms, and $|\tilde{p}_i^a\rangle$ are the PAW projector functions defined by Blöchl [33]. It should be noted that the term on the left hand side of equation 7.1 is not the full projection of $\langle\psi_m^A|$ onto $|\psi_n^{AQ}\rangle$ as might be inferred from the notation, but only the projection within the PAW spheres; it is, however, intuitive to write it in this way since it will be used as if it were the full projection. Other aspects of the notation presented here are the same as adopted in GPAW[133]. Because the quantities $\langle\psi_m^A|\tilde{p}_i^a\rangle$ and $\langle\tilde{p}_i^a|\psi_m^{AQ}\rangle$ are already calculated as part of any PAW code performing DFT on the systems of anthracene and AQ, respectively, they are readily available as output from those calculations.[134]

Since the projector functions are zero outside of the PAW spheres, they do not form a complete set over all of space, so that the resulting projections need to be normalized in a way that correctly indicates the degree to which the two states being compared can be considered as well represented by one another (i.e. they have sufficient overlap). We find reasonable results if we construct a normalization constant, *d_{mn}*, equal to the maximum of $\left|\left\langle\psi_m^A\middle|\psi_j^{AQ}\right\rangle\right|^2$ and $\left|\langle\psi_j^A|\psi_n^{AQ}\rangle\right|^2$, where *j* is varied over all of the KS states of AQ and anthracene, respectively, and use it to define a matrix representation of the MO diagram:

$$MO_{mn} = \frac{\left|\langle\psi_m^A|\psi_n^{AQ}\rangle\right|^2}{d_{mn}}. \tag{EQ 7.2}$$

For those states that are similar in spatial extent in the systems of AQ and A (one state from each system), one finds exclusively weight in the diagonal elements of the *MO* matrix, whereas states affected by the insertion of the functional groups are represented by rows with off-diagonal elements. The hybridization partners can then be read from the position of the non-zero elements in the row. As a consequence, the *MO* matrix can be compactly represented as an MO diagram. To simplify the diagrams, we additionally set values of MO_{mn} to 0 if they fall below some threshold. In this work the threshold was chosen to guarantee diagrams that would show important features in the electronic structure of each system while remaining relatively simple to interpret; these threshold values were 0.1 and 0.35 (out of a maximum of 1) for systems in vacuum and for adsorption systems respectively. Examples of these diagrams for AQ, DTA, and DSeA are in figures 7.2 and 7.3, the details of which are explained in sections 7.5 and 7.6 respectively. Each column of line segments shown represents a different MO matrix linking the states of the system on the left to those on the right.

7.5 Anthracene Derivative Orbitals in Vacuum

Figure 7.2 shows the relationships between KS orbitals of the A precursor and each of its derivatives which in section 7.6 are found to hybridize extensively with the Cu (111) surface

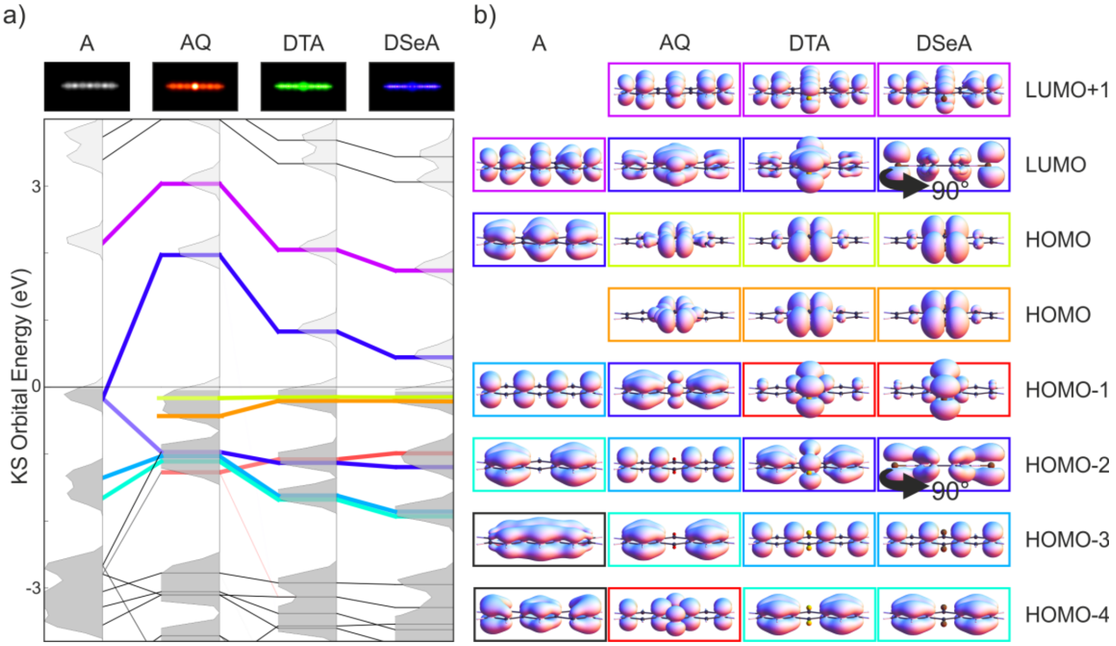

Figure 7.2 KS Orbitals of anthracene and its derivatives isolated in vacuum. **(a)** MO diagram highlighting similarities between the KS orbitals of each molecule. Column headings include total charge densities for each molecule in vacuum, integrated along the direction normal to the page and colored gray, red, green, and blue for A, AQ, DTA, DSeA respectively. The Fermi level is marked by a horizontal black line. States are color-coded according to the same scheme as in **(b)**. Surfaces of constant charge density (iso-surfaces) of the highest energy KS orbitals are displayed in **(b)**. Color-coded boxes surround related iso-surfaces of each molecule. The LUMO and HOMO-2 of DSeA appear the same as those of DTA, so are rotated 90° to illustrate the π anti-bonding/bonding nature of each with respect to their linkers.

upon adsorption (i.e. having many off-diagonal elements in the *MO* matrix). Figure 7.2(a) was generated using the implementation described in section 7.4, and as such serves as a first test-case of relatively simple systems whose orbital relationships can easily be verified by the human eye (see the surfaces of constant KS orbital charge density of figure 7.2(b)). The first column of figure 7.2(a) shows the density of states (DOS) of A. The second column shows the DOS of AQ. Between these two columns, lines connect the eigenvalues of KS states of A to those states of AQ that derive from them. Similarly, the DOS of each anthracene derivative is shown in its respective column, and the related states in each can be traced all the way (from right to left) back to their A precursor states. Those states that we consider to have some importance are color-coded according to figure 7.2(b). The order of color assignment for each state of each system is based on which states between systems are comparable (i.e. which states are linked together). For example, in figure 7.2(a) the LUMO of A can clearly be seen to connect to the LUMO+1 of AQ, therefore, both states are colored purple; comparison between the LUMO of A and the LUMO+1 of AQ in figure 7.2(b) shows that this assignment is correct. The introduction of warm colors (red, orange, and yellow) for the derived molecules is due to the presence of new states contributed from the linkers that do not exist in the A precursor (which has only cool colors in its color-coding). The HOMO-4 of AQ (red, second column) can be seen to derive somewhat from the A HOMO-4, but it is color-coded as a linker-derived state because the equivalent state in DTA and DSeA shows little relation to any state from A, as can be seen in the HOMO-1 states of figure 7.2(b) outlined in red. We treat the HOMO in the derived systems as being degenerate so it is assigned two colors (yellow and orange). The repetition of the color blue for the LUMO and HOMO-1 of AQ (HOMO-2 for DTA and DSeA) has the purpose of indicating that both of these states are derived from the HOMO of A.

As already noted, figure 7.2(a) could have been easily created by direct inspection of the shape of the KS orbital densities of figure 7.2(b). In this regard, figure 7.2(a) serves as a proof of concept that the procedure described in section 7.4 is capable of making the right assignments, as well as establishing the similarities between all three anthracene derivatives and their relationship to the A precursor. Figure 7.2(b) also makes it clear that the A HOMO derived states (boxed in blue) are hybridizations with the p_z orbitals of the linkers, creating a π bonding and anti-bonding pair, with the effect that these states, while assigned to the A precursor, should also have properties related to the linkers.

7.6 Results: Adsorbed System Orbital Comparisons

Having established the effectiveness of the technique described in section 7.4, we now turn to application of this MO analysis to systems exhibiting a continuum of states where such an automated analysis becomes indispensible. Figure 7.3 shows comparisons between the adsorption of (a) AQ and DTA, and (b) AQ and DSeA, and is arranged in a similar manner to figure 7.2(a), with the central DOS graphs of each being the projected density of states (PDOS) onto the adsorbate atoms (i.e. excluding PDOS of the underlying Cu) of the adsorbed systems.

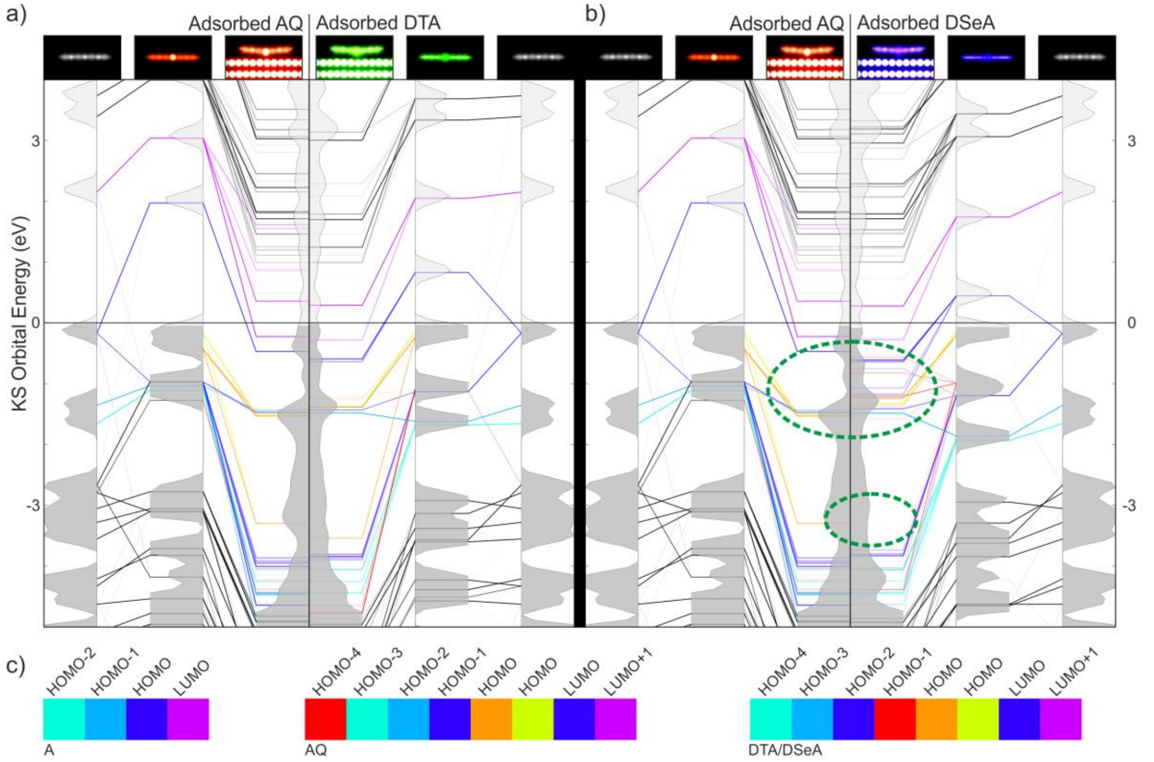

Figure 7.3 Side-by-side MO comparisons of **(a)** AQ and DTA, and **(b)** AQ and DSeA. The first three columns of DOS/PDOS are of the systems A in vacuum, AQ in vacuum, and AQ adsorbed to Cu (111) respectively, indicated by column headings showing the total charge density of those systems, integrated and colored as in figure 7.2. Dashed ovals in **(b)** highlight MOs that differ for DSeA when compared to the other two derivatives. Color-codes for each orbital as defined in figure 7.2 are repeated in **(c)** for reference.

The orbital color-codes introduced in figure 7.2 are used again here, and indicated in figure 7.3(c) for convenience. The first 2 columns of figure 7.3(a) are a repeat of the first 2 columns of figure 7.2(a) (showing how the states of AQ are derived from those of A).

The third column of figure 7.3(a) illustrates how the KS orbitals of an isolated molecule of AQ hybridize with the underlying Cu to create the states of the adsorbed AQ system. Similarly, the fourth column, shows how the KS orbitals of an isolated molecule of DTA hybridize to create the states of the adsorbed DTA system (if read from right to left). The fifth and sixth columns are arranged as mirror images of the second and first columns respectively, but now applied to DTA rather than AQ. This setup allows for a direct comparison of the adsorbed system KS orbitals of AQ and DTA. Figure 7.3(b) repeats the same structure, but now for direct comparison of adsorbed AQ (left) to adsorbed DSeA (right).

Close inspection of the third and fourth columns of figure 7.3(a) shows that the bonding of AQ and DTA to the surface is quite comparable, particularly for states below E_F: while the precise KS eigenvalues often vary slightly between the two, they appear to have a near one-to-one correspondence. Figure 7.3(b) however, shows that this is not the case when comparing adsorbed AQ to adsorbed DSeA (and by transitivity, when comparing DTA to DSeA). In particular, DSeA shows significantly more hybridization of its LUMO, HOMO-1, and HOMO-2 (blue, red, and blue again, respectively) in the range of -1.5 eV to 0 eV (circled). Furthermore DSeA shows no signs of bonding of its HOMO to lower energy states (below -3 eV), whereas AQ and DTA do. Experimentally we observe such a low diffusion barrier (< 20 meV) for DSeA that its motion cannot be frozen out at the lowest temperatures provided by our STM (between 10 and 20 K, see figure 7.4). This is a significantly lower diffusion barrier when compared to those previously reported for AQ[81] and DTA[125] (23 meV and 130 meV respectively) the motions of

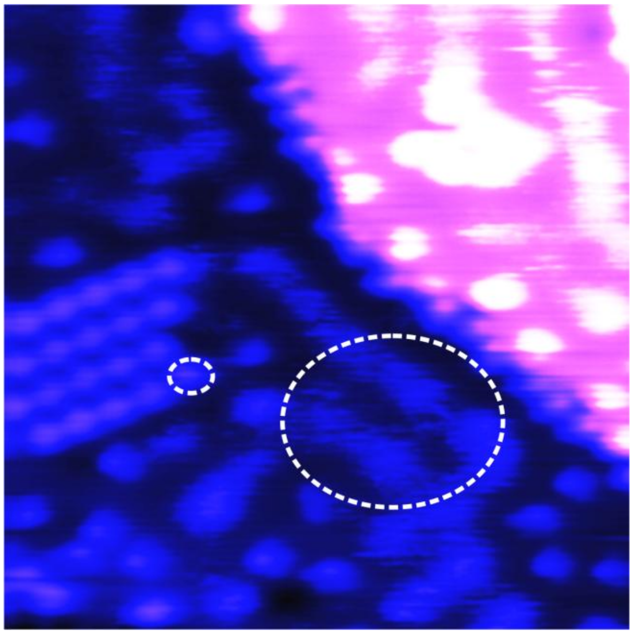

Figure 7.4 STM scan of DSeA on Cu (111) showing that individual DSeA molecules cannot be isolated by themselves under imaging conditions. Individuals can only be imaged when trapped as part of an island of DSeA (e.g. small circle), or when decorating a step edge, while on the open terrace individuals appear as motion blurs (e.g. large circle); therefore the diffusion barrier of DSeA lies below the temperature resolution of the instrument. Scanning parameters: 14 nm x 14 nm, Bias = -1.5 V, Current = 66 pA.

which could be frozen out by our equipment. Based on the circled differences in figure 7.3(b), we therefore assign DSeA's lower diffusion barrier to be related to its linkers' tendency to bind at higher energies than its counterparts, as well as the somewhat different hybridization behavior of its LUMO.

According to figure 7.3(a) then, AQ should exhibit similar diffusion behavior to DTA; however, as already noted, the apparent barrier for AQ is much smaller than that of DTA. In this case we believe the deciding factor is that the O linkers of AQ, unlike its more massive chalcogen counterparts of S and Se, are able to tunnel through part of the diffusion barrier, thereby circumventing the constraints placed on it by bonds that are otherwise quite similar to those of DTA; the fact that AQ's linker-derived HOMO-4 state, unlike its DTA and DSeA counterparts, inherits charge density from A's HOMO-4 π system state (see figure 7.2(a,b)) may also play a role in this. In previous studies of similar uniaxially diffusing molecules we have also observed such apparent tunneling behavior for O linkers.[135]

7.7 Conclusions

In conclusion we have demonstrated a way to extract MO diagrams from typical DFT codes employing PAW bases for a variety of related systems that enables facile side-by-side comparison of their chemical properties within an MO theory-based framework. Using this technique we were able to trace the orbitals of anthracene derivatives from their beginnings as anthracene orbitals and linker orbitals to their final configurations upon adsorption of each derivative. In doing so, we found that DSeA in particular exhibits a different bonding behavior with respect to its linker-related states, which then provides a chemical explanation for STM results showing that DSeA has the lowest diffusion barrier among the three derivatives studied.

Chapter 8

Conclusions and Future Work

8.1 Conclusions

The studies presented in this dissertation all focused on systems whose important features extend over a very small spatial range: over angstroms and nanometers. Before they were ever conceived of or observed in the Bartels lab, and before I (and others) analyzed them, at a most fundamental level they were already well-understood: each system consisting of atoms, electrons, molecules, and nanometer scale superstructures is for most intents and purposes perfectly described by the Schrödinger equation. So if we already know everything about these systems, why study them – what more can we learn?

The answer (aside from 42 [136]) is that, in isolation, the raw information we get from a brute-force application of Quantum Mechanics is not practical. This is true both in terms of the computational resources required (as the system size grows), as well as how useful the information about the system is to us once we have it. Our goal should be to simplify and distil out only the information and insights that will allow us to make useful predictions about these and related systems (as well as helping us to decide what it means for systems to be related in the first place). This is what my co-workers and I have tried to do in each of the cases studied in this dissertation, for the general class of systems described as “organic molecules adsorbed to a Cu (111) surface”.

8.2 Future Work

In this section I would like to propose what I believe the next logical step should be with regards to interpreting the physical meaning of KS orbitals, as related to the analysis performed in Chapter 7. As noted in Chapter 1, the KS orbitals are considered to be an auxiliary mathematical system used as a tool to solve the real problem in DFT. However it is already common practice to treat KS orbitals as though they represent some real physical quantity (e.g. it is routine to use them to generate as DOS or PDOS plots). The main problem with these orbitals is that because they represent an auxiliary system of non-interacting single-particle electrons, their energy eigenvalues do not strictly represent a real energy in the way that we would want to interpret an energy eigenvalue (as being the energy of an actual particle, or quasi-particle). It has however been noted that the energy eigenvalues can often be rescaled to fit, for example, the HF orbital eigenvalues.[137] I believe that a deeper interpretation of their physical meaning lies in the charge density which they can be considered to partition (see below).

In Molecular Orbital (MO) theory, there is a concept of whether a particular orbital is "bonding" or "anti-bonding", the determination of which is often made on a geometric basis (does the charge distribution of this orbital help to hold 2 nuclei together, does it tend to push them apart, or does it have a neutral effect?). For complex systems (e.g. those studied in Chapter 7), this definition presents a problem because there are many nuclei and the question of bonding or anti-bonding needs to be asked with respect to what change is being made to the system. For example, one orbital that binds a molecule to a substrate might prefer to bind the molecule to one adsite while a different orbital might prefer to bind the molecule to a different adsite. What we would like then, is to take the potential energy surface (PES) associated with

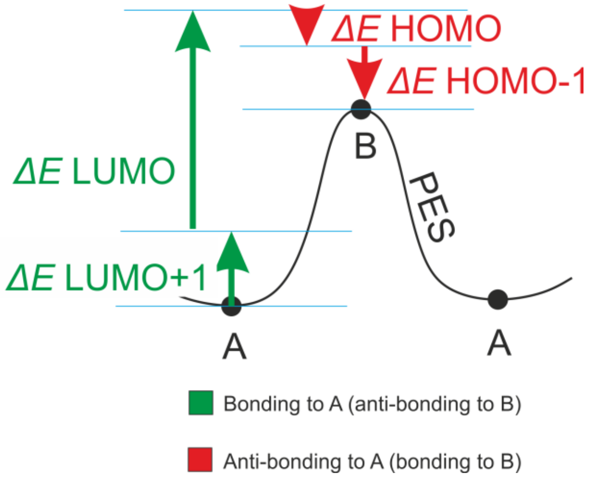

Figure 8.1 Partitioning of a PES barrier into energetic contributions from various KS states.

motion of each of the nuclii (ideally, easily calculated with DFT, though famously problematic for some systems [138]) and determine how each KS orbital contributes to that PES. In this way, for example, a diffusion barrier (see cartoon in figure 8.1) could be broken down into its energetic contributions from each KS orbital with orbitals that contribute positively to that barrier considered as bonding with respect to the preferred adsite and with those orbitals contributing negatively to the barrier considered as anti-bonding with respect to the preferred adsite (or, equivalently, bonding with respect to the transition state). This would yield a quantitative energetic meaning to each KS state (or, more generally, any chosen partitioning of the charge density). In what follows I show how this might be done.

Based on the Hellman-Feynman theorem, the ground state charge density can be evaluated directly as an electrostatic charge distribution in order to calculate the force on each nucleus (or ion in a frozen-core approximation) in a given system. In this way, one can in principle calculate the energy difference between, for example, two different adsorption configurations (call them A and B) of a molecule undergoing diffusion (i.e. we are considering the PES at two points A and B). One would do this by dividing up the path from A to B into differential changes of the positions of the nuclii, and calculate the work done in forcing the ions to move from configuration A to B:

$$\begin{aligned} E_A - E_B = \Delta E_{A\to B} \quad &= \sum_i \int_A^B dx_i \, F_{x_i} \\ &= \sum_i \int_A^B \big(dx_i (F_{x_i}^{elec}[n_0] + F_{x_i}^{nuc}) \big), \qquad \text{(EQ 8.1)} \end{aligned}$$

where the index i runs over each of the nuclii coordinates x_i , the force on the nucleus at each such point being F_{x_i} which is then divided into a contribution from the ground state electron density $F_{x_i}^{elec}[n_0]$ evaluated at each differential configuration and a contribution from the repulsion due to the surrounding nuclii $F_{x_i}^{nuc}$. Of course, the energy difference between A and B could just as well be solved by taking the difference in the ground state energy calculated by DFT for the system in both configurations – what has been gained by this alternative approach is that the energy has been written in a way that can be partitioned by the KS orbitals: $F_{x_i}^{elec}$ is linear with respect to partitioning of the charge density, therefore we may define the force on each ion due to the occupied KS orbital $|\varepsilon\rangle$ as $F_{x_i}^{\varepsilon} \equiv F_{x_i}^{elec}[n_\varepsilon]$ where $n_\varepsilon(\vec{r}) = |\langle \vec{r}|\varepsilon\rangle|^2$. That is,

$$F_{x_i}^{elec}[n_0] = F_{x_i}^{elec}\left[\sum_\varepsilon n_\varepsilon\right] = \sum_\varepsilon F_{x_i}^{elec}[n_\varepsilon] = \sum_\varepsilon F_{x_i}^{\varepsilon}.$$

We can just as well consider the force associated with an orbital $|e\rangle$ from the related molecule-in-vacuum system (e.g. in Chapter 7 I spoke of the projection of the HOMO etc. of AQ onto the adsorbed AQ system), $F_{x_i}^{e,\varepsilon} \equiv \langle\varepsilon|e\rangle\langle e|\varepsilon\rangle F_{x_i}^{\varepsilon}$ so that $F_{x_i}^{\varepsilon} = \sum_e F_{x_i}^{e,\varepsilon}$. Because $|e\rangle$ is fixed with respect to the changing adsorption system (in going from A to B) substitution back into equation 8.1 yields quantities (call them $\Delta E^{e}_{A\to B}$) very similar to what we would like to have:

$$\begin{aligned} E_A - E_B \quad &= \sum_e \Delta E^{e}_{A\to B} + \sum_i \int_A^B dx_i\, F^{nuc}_{x_i} \\ &= \sum_e \left\{ \sum_i \int_A^B \left(\sum_\varepsilon dx_i\, F^{e,\varepsilon}_{x_i} \right) \right\} + \sum_i \int_A^B dx_i\, F^{nuc}_{x_i} \ , \end{aligned}$$

where the expression for $\Delta E^{e}_{A\to B}$ is given by the term in curly-brackets above. This is already a perfectly good and physically interpretable partitioning of the barrier energy (if A is taken to be the optimum configuration and B the transition configuration) into parts due to the $|e\rangle$ states and one big part due to the nuclii repulsions. What I believe would be more faithful to the original concept of bonding/anti-bonding would be to consider the effective energy that a KS orbital contributes to the barrier with the idea that each orbital must pull its figurative weight in opposing the repulsions of the nuclii (given N occupied states): $F^{\varepsilon-eff}_{x_i} \equiv F^{\varepsilon}_{x_i} + \frac{1}{N} F^{nuc}_{x_i}$, $F^{e,\varepsilon-eff}_{x_i} \equiv \langle\varepsilon|e\rangle\langle e|\varepsilon\rangle F^{\varepsilon-eff}_{x_i}$, and

$$E_A - E_B \quad = \sum_e \Delta E^{e-eff}_{A\to B} \ = \sum_e \left\{ \sum_i \int_A^B \left(\sum_\varepsilon dx_i\, F^{e,\varepsilon-eff}_{x_i} \right) \right\},$$

where, as was the case before, $\Delta E^{e-eff}_{A\to B}$ is given by the term in curly-brackets. Now for each molecule state $|e\rangle$ (LUMO, HOMO, etc.), an energy contribution to the barrier can be defined to create a picture like figure 8.1, yielding at the same time a quantitative interpretation of the MO type analysis presented in Chapter 7, as well as of the KS orbitals themselves.

References

[1] Pawin G, Wong K L, Kwon K Y and Bartels L 2006 A homomolecular porous network at a Cu(111) surface *Science* **313** 961-2

[2] Ennis C J, Carr P A and McCash E M 2003 Long range ordered structure of ethyne on Cu(111) *Surf. Sci.* **539** L574-L6

[3] Zhu Y, Wyrick J, Cohen K D, Magnone K M, Holzke C, Salib D, Ma Q, Sun D and Bartels L 2012 Acetylene on Cu(111): imaging a molecular surface arrangement with a constantly rearranging tip *J. Phys.-Condens. Mat.* **24** 354005

[4] Wyrick J, Kim D, Sun D, Cheng Z, Lu W, Zhu Y, Berland K, Kim Y, Rotenberg E, Luo M, Hyldgaard P, Einstein T L and Bartels L 2011 Do two-dimensional "noble gas atoms" produce molecular honeycombs at a metal surface? *Nano Lett* **11** 2944-8

[5] Cheng Z, Wyrick J, Luo M, Sun D, Kim D, Zhu Y, Lu W, Kim K, Einstein T L and Bartels L 2010 Adsorbates in a Box: Titration of Substrate Electronic States *Phys. Rev. Lett.* **105** 066104

[6] Cheng Z, Luo M, Wyrick J, Sun D, Kim D, Zhu Y, Lu W, Kim K, Einstein T L and Bartels L 2010 Power of Confinement: Adsorbate Dynamics on Nanometer-Scale Exposed Facets *Nano Lett* **10** 3700-3

[7] Hohenberg P and Kohn W 1964 Inhomogeneous Electron Gas *Phys. Rev. B* **136** B864-&

[8] Kohn W and Sham L J 1965 Self-consistent equations including exchange and correlation effects *Phys. Rev.* **140** A1133-A8

[9] Bickelhaupt F M and Baerends E J 2000 Kohn-Sham density functional theory: Predicting and understanding chemistry *Reviews in Computational Chemistry, Vol 15* **15** 1-86

[10] Kummel S and Kronik L 2008 Orbital-dependent density functionals: Theory and applications *Rev. Mod. Phys.* **80** 3-60

[11] Dreizler R M and Gross E K U 1990 *Density Functional Theory: an Approach to the Quantum Many-Body Problem* (Berlin: Springer)

[12] Sholl D S and Steckel J A 2009 *Density Functional Theory*: John Wiley & Sons, Inc.) pp 1-238

[13] Engel E and Dreizler R M 2011 *Density Functional Theory: an Advanced Course* (Berlin: Springer)

[14] Tersoff J and Hamann D R 1985 Theory of the scanning tunneling microscope *Phys. Rev. B* **31** 805-13

[15] Bracher C, Riza M and Kleber M 1997 Propagator theory of scanning tunneling microscopy *Phys. Rev. B* **56** 7704-15

[16] Christensen C H, Rass-Hansen J, Marsden C C, Taarning E and Egeblad K 2008 The renewable chemicals industry *Chemsuschem* **1** 283-9

[17] Bao S, Schindler K M, Hofmann P, Fritzsche V, Bradshaw A M and Woodruff D P 1993 The local adsorption structure of acetylene on Cu(111) *Surf. Sci.* **291** 295-308

[18] Hermann K and Witko M 1995 Geometry and binding of acetylene on Cu(111): ab initio cluster studies *Surf. Sci.* **337** 205-14

[19] Konishi Y, Sainoo Y, Kanazawa K, Yoshida S, Taninaka A, Takeuchi O and Shigekawa H 2005 Tunneling spectroscopy and manipulation of a single C2H2 molecule on a Cu(111) surface *Phys. Rev. B* **71** 193410

[20] Stipe B, Rezaei M and Ho W 1998 Single-molecule vibrational spectroscopy and microscopy *Science* **280** 1732-5

[21] Eigler D, Lutz C and Rudge W 1991 An atomic switch realized with the scanning tunneling microscope *Nature* **352** 600-3

[22] Neu B, Meyer G and Rieder K 1995 Controlled vertical and lateral manipulation of single atoms and molecules with the scanning tunneling microscope *Mod Phys Lett B* **9** 963-9

[23] Bartels L, Meyer G and Rieder K 1997 Controlled vertical manipulation of single CO molecules with the scanning tunneling microscope: A route to chemical contrast *Appl. Phys. Lett.* **71** 213-5

[24] Hahn J and Ho W 2001 Single molecule imaging and vibrational spectroscopy with a chemically modified tip of a scanning tunneling microscope *Phys. Rev. Lett.* **8719** 196102

[25] Gross L, Moll N, Mohn F, Curioni A, Meyer G, Hanke F and Persson M 2011 High-resolution molecular orbital imaging using a p-wave STM tip *Phys. Rev. Lett.* **107** 086101

[26] Gingery D and Buhlmann P 2011 Voltage-induced chemical contrast in scanning tunneling microscopy using tips chemically modified with hydrogen bond donors *Surf. Sci.* **605** 1099-102

[27] Kresse G and Hafner J 1993 Abinitio molecular-dynamics for liquid-metals *Phys. Rev. B* **47** 558-61

[28] Kresse G and Hafner J 1994 Ab-initio molecular-dynamics simulation of the liquid-metal amorphous-semiconductor transition in germanium *Phys. Rev. B* **49** 14251-69

[29] Kresse G and Furthmuller J 1996 Efficiency of ab-initio total energy calculations for metals and semiconductors using a plane-wave basis set *Comp Mater Sci* **6** 15-50

[30] Kresse G and Furthmuller J 1996 Efficient iterative schemes for ab initio total-energy calculations using a plane-wave basis set *Phys. Rev. B* **54** 11169-86

[31] Perdew J P, Burke K and Ernzerhof M 1996 Generalized gradient approximation made simple *Phys. Rev. Lett.* **77** 3865-8

[32] Perdew J P, Burke K and Ernzerhof M 1997 Erratum: Generalized gradient approximation made simple (vol 77, pg 3865, 1996) *Phys. Rev. Lett.* **78** 1396

[33] Blochl P E 1994 Projector Augmented-Wave Method *Phys. Rev. B* **50** 17953-79

[34] Kresse G and Joubert D 1999 From ultrasoft pseudopotentials to the projector augmented-wave method *Phys. Rev. B* **59** 1758-75

[35] Sautet P and Bocquet M L 1994 A theoretical-analysis of the site dependence of the shape of a molecule in STM images *Surf. Sci.* **304** L445-L50

[36] Pedersen M, Bocquet M, Sautet P, Laegsgaard E, Stensgaard I and Besenbacher F 1999 CO on Pt(111): binding site assignment from the interplay between measured and calculated STM images *Chem. Phys. Lett.* **299** 403-9

[37] Tiwari R K, Otalvaro D M, Joachim C and Saeys M 2009 Origin of the contrast inversion in the STM image of CO on Cu *Surf. Sci.* **603** 3286-91

[38] Nieminen J, Niemi E, Simic-Milosevic V and Morgenstern K 2005 STM images and tunneling channels of substituted benzene molecules *Phys. Rev. B* **72** 195421

[39] Luo M, Lu W, Kim D, Chu E, Wyrick J, Holzke C, Salib D, Cohen K D, Cheng Z, Sun D, Zhu Y, Einstein T L and Bartels L 2011 Coalescence of 3-phenyl-propynenitrile on Cu(111) into interlocking pinwheel chains *J. Chem. Phys.* **135** 134705

[40] Repp J, Moresco F, Meyer G, Rieder K H, Hyldgaard P and Persson M 2000 Substrate mediated long-range oscillatory interaction between adatoms: Cu/Cu(111) *PHYSICAL REVIEW LETTERS* **85** 2981-4

[41] Knorr N, Brune H, Epple M, Hirstein A, Schneider M and Kern K 2002 Long-range adsorbate interactions mediated by a two-dimensional electron gas *Phys. Rev. B* **65** 115420

[42] Mitsui T, Rose M K, Fomin E, Ogletree D F and Salmeron M 2005 Diffusion and pair interactions of CO molecules on Pd(111) *Phys. Rev. Lett.* **94** 036101

[43] Wong K L, Rao B V, Pawin G, Ulin-Avila E and Bartels L 2005 Coverage and nearest-neighbor dependence of adsorbate diffusion *J. Chem. Phys.* **123** 201102

[44] Wang Y F, Ge X, Manzano C, Korger J, Berndt R, Hofer W A, Tang H and Cerda J 2009 Supramolecular patterns controlled by electron interference and direct intermolecular interactions *J. Am. Chem. Soc.* **131** 10400-2

[45] Silly F, Pivetta M, Ternes M, Patthey F, Pelz J P and Schneider W D 2004 Creation of an atomic superlattice by immersing metallic adatoms in a two-dimensional electron sea *Phys. Rev. Lett.* **92** 016101

[46] Stepanyuk V S, Niebergall L, Baranov A N, Hergert W and Bruno P 2006 Long-range electronic interactions between adatoms on transition metal surfaces *Comp Mater Sci* **35** 272-4

[47] Stranick S J, Kamna M M and Weiss P S 1994 Atomic-scale dynamics of a 2-dimensional gas-solid interface *Science* **266** 99-102

[48] Kulawik M, Rust H P, Heyde M, Nilius N, Mantooth B A, Weiss P S and Freund H J 2005 Interaction of CO molecules with surface state electrons on Ag(111) *Surf. Sci.* **590** L253-L8

[49] Sykes E C H, Han P, Kandel S A, Kelly K F, McCarty G S and Weiss P S 2003 Substrate-mediated interactions and intermolecular forces between molecules adsorbed on surfaces *Acc. Chem. Res.* **36** 945-53

[50] Nanayakkara S U, Sykes E C H, Fernandez-Torres L C, Blake M M and Weiss P S 2007 Long-range electronic interactions at a high temperature: bromine adatom islands on Cu(111) *Phys. Rev. Lett.* **98** 206108-4

[51] Lukas S, Witte G and Woll C 2002 Novel mechanism for molecular self-assembly on metal substrates: Unidirectional rows of pentacene on Cu(110) produced by a substrate-mediated repulsion *Phys. Rev. Lett.* **88** 028301

[52] Einstein T L 1996 *Physical structure of solid surfaces, Handbook of surface science ; v. 1,* ed W N Unertl (Amsterdam ; New York: Elsevier) pp 577-650

[53] Fichthorn K and Scheffler M 2000 Island nucleation in thin-film epitaxy: A first-principles investigation *Phys. Rev. Lett.* **84** 5371-4

[54] Österlund L, Pedersen M, Stensgaard I, Laesgaard E and Besenbacher F 1999 Quantitative determination of adsorbate-adsorbate interactions *Phys. Rev. Lett.* **83** 4812-5

[55] Han P and Weiss P S 2012 Electronic substrate-mediated interactions *Surf Sci Rep* **67** 19-81

[56] Hyldgaard P and Persson M 2000 Long-ranged adsorbate-adsorbate interactions mediated by a surface-state band *J. Phys.-Condens. Mat.* **12** L13-L9

[57] Kevan S D and Gaylord R H 1987 High-resolution photoemission study of the electronic structure of the noble-metal (111) surfaces *Phys. Rev. B* **36** 5809-18

[58] Berland K, Einstein T L and Hyldgaard P 2012 Response of the Shockley surface state to an external electrical field: A density-functional theory study of Cu(111) *Phys. Rev. B* **85** 035427

[59] Hasegawa Y and Avouris P 1993 Direct Observation of Standing-Wave Formation at Surface Steps Using Scanning Tunneling Spectroscopy *Phys. Rev. Lett.* **71** 1071-4

[60] Crommie M, Lutz C and Eigler D 1993 Imaging Standing Waves in a 2-Dimensional Electron-gas *Nature* **363** 524-7

[61] Li J, Schneider W, Berndt R and Crampin S 1998 Electron confinement to nanoscale Ag islands on Ag(111): A quantitative study *Phys. Rev. Lett.* **80** 3332-5

[62] Heller E, Crommie M, Lutz C and Eigler D 1994 Scattering and Adsorption of Surface Electron Waves in Quantum Corrals *Nature* **369** 464-6

[63] Li J, Schneider W, Crampin S and Berndt R 1999 Tunnelling spectroscopy of surface state scattering and confinement *Surf. Sci.* **422** 95-106

[64] Rieder K, Meyer G, Hla S, Moresco F, Braun K, Morgenstern K, Repp J, Foelsch S and Bartels L 2004 The scanning tunnelling microscope as an operative tool: doing physics and chemistry with single atoms and molecules *PHILOS T ROY SOC A* **362** 1207-16

[65] Manoharan H, Lutz C and Eigler D 2000 Quantum mirages formed by coherent projection of electronic structure *Nature* **403** 512-5

[66] Repp J, Moresco F, Meyer G, Rieder K, Hyldgaard P and Persson M 2000 Substrate mediated long-range oscillatory interaction between adatoms: Cu/Cu(111) *Phys. Rev. Lett.* **85** 2981-4

[67] Stepanyuk V, Baranov A, Tsivlin D, Hergert W, Bruno P, Knorr N, Schneider M and Kern K 2003 Quantum interference and long-range adsorbate-adsorbate interactions *Phys. Rev. B* **68** 205410

[68] Wang Y F, Ge X, Manzano C, Korger J, Berndt R, Hofer W A, Tang H and Cerda J 2009 Supramolecular Patterns Controlled by Electron Interference and Direct Intermolecular Interactions *J. Am. Chem. Soc.* **131** 10400-+

[69] Sykes E, Han P, Kandel S, Kelly K, McCarty G and Weiss P 2003 Substrate-mediated interactions and intermolecular forces between molecules adsorbed on surfaces *Acc. Chem. Res.* **36** 945-53

[70] Kuehne D, Klappenberger F, Krenner W, Klyatskaya S, Ruben M and Barth J V 2010 Rotational and constitutional dynamics of caged supramolecules *Proc. Natl. Acad. Sci. USA* **107** 21332-6

[71] Pawin G, Solanki U, Kwon K Y, Wong K L, Lin X, Jiao T and Bartels L 2007 A Quantitative Approach to Hydrogen Bonding at a Metal Surface *J. Am. Chem. Soc.* **129** 12056 -7

[72] Tsong T T and Casanova R 1981 Direct Measurement of Pair Energies in Adatom-Adatom Interactions on a Metal-Surface *Phys. Rev. B* **24** 3063-72

[73] Hyldgaard P and Einstein T L 2005 Interactions mediated by surface states: from pairs and trios to adchains and ordered overlayers *J. Crys. Growth* **275** e1637-e42

[74] Kellogg G L 1994 Field-Ion Microscope Studies of Single-Atom Surface-Diffusion and Cluster Nucleation on Metal-Surfaces *SURF SCI REP* **21** 1-88

[75] Fink H W and Ehrlich G 1984 Pair and Trio Interactions between Adatoms - Re on W(110) *J. Chem. Phys.* **81** 4657-65

[76] Kim K and Einstein T L 2011 Monte Carlo study of the honeycomb structure of anthraquinone molecules on Cu(111) *Phys. Rev. B* **in press**

[77] Lobo-Checa J, Matena M, Muller K, Dil J H, Meier F, Gade L H, Jung T A and Stohr M 2009 Band Formation from Coupled Quantum Dots Formed by a Nanoporous Network on a Copper Surface *Science* **325** 300-3

[78] Gross L, Moresco F, Savio L, Gourdon A, Joachim C and Rieder K 2004 Scattering of surface state electrons at large organic molecules *Phys. Rev. Lett.* **93** 056103

[79] Klappenberger F, Kuhne D, Krenner W, Silanes I, Arnau A, de Abajo F J G, Klyatskaya S, Ruben M and Barth J V 2011 Tunable Quantum Dot Arrays Formed from Self-Assembled Metal-Organic Networks *Phys. Rev. Lett.* **106** 026802

[80] Morgenstern K, Laegsgaard E and Besenbacher F 2005 Quantum size effects in adatom island decay *Phys. Rev. Lett.* **94** 166104

[81] Wong K L, Pawin G, Kwon K Y, Lin X, Jiao T, Fawcett R, Solanki U, Bartels L, Stolbov S and Rahman T S 2007 A Molecule Carrier *Science* **315** 1391-3

[82] http://www.camp.dtu.dk/software.aspx/Dacapo/.

[83] Lee K, Murray E D, Kong L Z, Lundqvist B I and Langreth D C 2010 Higher-accuracy van der Waals density functional *Phys. Rev. B* **82** 081101

[84] Dion M, Rydberg H, Schröder E, Langreth D C and Lundqvist B I 2004 Van der Waals density functional for general geometries *Phys. Rev. Lett.* **92** 246401

[85] Fiete G A and Heller E J 2003 Colloquium: Theory of quantum corrals and quantum mirages *Rev. Mod. Phys.* **75** 933-48

[86] Kevan S D and Gaylord R H 1987 High-Resolution Photoemission-Study of the Electronic-Structure of the Noble-Metal (111) Surfaces *Phys. Rev. B* **36** 5809-18

[87] Scheybal A, Muller K, Bertschinger R, Wahl M, Bendounan A, Aebi P and Jung T A 2009 Modification of the Cu(110) Shockley surface state by an adsorbed pentacene monolayer *Phys. Rev. B* **79** 115406

[88] Fock V 1928 Bemerkungen zur Quantelung des harmonischen Oscillators im Magnetfeld *Zeitschrift für Physik* **47** 446-8

[89] Kouwenhoven L and Marcus C 1998 Quantum dots *Physics World* **11** 35-9

[90] Kouwenhoven L P, Austing D G and Tarucha S 2001 Few-electron quantum dots *Rep. Prog. Phys.* **64** 701-36

[91] Darwin C G 1930 The diamagnetism of the free electron. *Proceedings of the Cambridge Philosophical Society* **27** 86-90

[92] Villain J 1980 *Ordering in strongly fluctuating condensed matter systems,* ed T Riste (New York: Plenum Press) pp 221-60

[93] Haruta M 2005 Catalysis - Gold rush *Nature* **437** 1098-9

[94] Bartels L 2010 Tailoring molecular layers at metal surfaces *Nature Chemistry* **2** 87-95

[95] Corso M, Auwarter W, Muntwiler M, Tamai A, Greber T and Osterwalder J 2004 Boron nitride nanomesh *Science* **303** 217-20

[96] Rastei M V, Heinrich B, Limot L, Ignatiev P A, Stepanyuk V S, Bruno P and Bucher J P 2007 Size-dependent surface states of strained cobalt nanoislands on Cu(111) *Phys. Rev. Lett.* **99** -

[97] Theobald J A, Oxtoby N S, Phillips M A, Champness N R and Beton P H 2003 Controlling molecular deposition and layer structure with supramolecular surface assemblies *Nature* **424** 1029-31

[98] Berner S, Corso M, Widmer R, Groening O, Laskowski R, Blaha P, Schwarz K, Goriachko A, Over H, Gsell S, Schreck M, Sachdev H, Greber T and Osterwalder J 2007 Boron nitride nanomesh: Functionality from a corrugated monolayer *Angew. Chem. Int. Ed. Engl.* **46** 5115-9

[99] Gsell M, Jakob P and Menzel D 1998 Effect of substrate strain on adsorption *Science* **280** 717-20

[100] Negulyaev N N, Stepanyuk V S, Niebergall L, Bruno P, Hergert W, Repp J, Rieder K H and Meyer G 2008 Direct Evidence for the Effect of Quantum Confinement of Surface-State Electrons on Atomic Diffusion *Phys. Rev. Lett.* **101** -

[101] WATANABE F and EHRLICH G 1991 DIRECT OBSERVATIONS OF PAIR INTERACTIONS ON A METAL - HETEROPAIRS ON W(110) *J. Chem. Phys.* **95** 6075-87

[102] Hyldgaard P and Einstein T L 2002 Surface-state mediated three-adsorbate interaction *Europhys. Lett.* **59** 265-71

[103] Bogicevic A, Ovesson S, Hyldgaard P, Lundqvist B I, Brune H and Jennison D R 2000 Nature, strength, and consequences of indirect adsorbate interactions on metals *Phys. Rev. Lett.* **85** 1910-3

[104] Mathews J and Walker R L 1970 *Mathematical methods of physics* (New York,: W. A. Benjamin)

[105] Atkinson K E and Han W 2004 *Elementary numerical analysis* (Hoboken, NJ: J. Wiley & Sons)

[106] Kiełbasiński A and Schwetlick H 1988 *Numerische lineare Algebra : eine computerorientierte Einführung* (Thun [etc.]: Harri Deutsch)

[107] Burgi L, Petersen L, Brune H and Kern K 2000 Noble metal surface states: deviations from parabolic dispersion *Surf. Sci.* **447** L157-L61

[108] Haruta M, Kobayashi T, Sano H and Yamada N 1987 Novel Gold Catalysts for the Oxidation of Carbon-Monoxide at a Temperature Far Below 0-Degrees-C *Chemistry Letters* 405-8

[109] Chen M S and Goodman D W 2004 The structure of catalytically active gold on titania *Science* **306** 252-5

[110] Somorjai G A 1994 *Introduction to surface chemistry and catalysis* (New York: Wiley)

[111] Mantooth B A, Sykes E C H, Han P, Moore A M, Donhauser Z J, Crespi V H and Weiss P S 2007 Analyzing the motion of benzene on Au{111}: Single molecule statistics from scanning probe images *J. Phys. Chem. C* **111** 6167-82

[112] Han P, Mantooth B, Sykes E, Donhauser Z and Weiss P 2004 Benzene on Au (111) at 4 K: Monolayer growth and tip-induced molecular cascades *J. Am. Chem. Soc.* **126** 10787-93

[113] Sachs C, Hildebrand M, Volkening S, Wintterlin J and Ertl G 2001 Spatiotemporal self-organization in a surface reaction: From the atomic to the mesoscopic scale *Science* **293** 1635-8

[114] Hendriksen B, Bobaru S and Frenken J 2004 Oscillatory CO oxidation on Pd(100) studied with in situ scanning tunneling microscopy *Surf. Sci.* **552** 229-42

[115] Tierney H L, Baber A E and Sykes E C H 2009 Atomic-Scale Imaging and Electronic Structure Determination of Catalytic Sites on Pd/Cu Near Surface Alloys *J. Phys. Chem. C* **113** 7246-50

[116] Briner B, Doering M, Rust H and Bradshaw A 1997 Microscopic molecular diffusion enhanced by adsorbate interactions *Science* **278** 257-60

[117] Heinrich A, Lutz C, Gupta J and Eigler D 2002 Molecule cascades *Science* **298** 1381-7

[118] Longwitz S, Schnadt J, Vestergaard E, Vang R, Laegsgaard E, Stensgaard I, Brune H and Besenbacher F 2004 High-coverage structures of carbon monoxide adsorbed on Pt(111) studied by high-pressure scanning tunneling microscopy *J. Phys. Chem. B* **108** 14497-502

[119] Stepanow S, Lingenfelder M, Dmitriev A, Spillmann H, Delvigne E, Lin N, Deng X B, Cai C Z, Barth J V and Kern K 2004 Steering molecular organization and host-guest interactions using two-dimensional nanoporous coordination systems *Nat. Mater.* **3** 229-33

[120] Decker R, Schlickum U, Klappenberger F, Zoppellaro G, Klyatskaya S, Ruben M, Barth J V and Brune H 2008 Using metal-organic templates to steer the growth of Fe and Co nanoclusters *Appl. Phys. Lett.* **93** 243102

[121] Otero R, Rosei F, Naitoh Y, Jiang P, Thostrup P, Gourdon A, Laegsgaard E, Stensgaard I, Joachim C and Besenbacher F 2004 Nanostructuring Cu surfaces using custom-designed molecular molds *Nano Lett* **4** 75-8

[122] Static Confinement of CO in much larger edge-pits has been investigated by Kulawik et al., Surf. Sci. 590, L53 (2005)

[123] Bartels L, Meyer G and Rieder K 1999 The evolution of CO adsorption on Cu(111) as studied with bare and CO-functionalized scanning tunneling tips *Surf. Sci.* **432** L621-L6

[124] Shan B, Zhao Y J, Hyun J, Kapur N, Nicholas J B and Cho K 2009 Coverage-Dependent CO Adsorption Energy from First-Principles Calculations *J. Phys. Chem. C* **113** 6088-92

[125] Kwon K Y, Wong K L, Pawin G, Bartels L, Stolbov S and Rahman T S 2005 Unidirectional adsorbate motion on a high-symmetry surface: "Walking" molecules can stay the course *Phys. Rev. Lett.* **95** 166101

[126] Smith M B and Michl J 2013 *Annual Review of Physical Chemistry, Vol 64,* ed M A Johnson and T J Martinez pp 361-86

[127] Zheng C J, Zhao W M, Wang Z Q, Huang D, Ye J, Ou X M, Zhang X H, Lee C S and Lee S T 2010 Highly efficient non-doped deep-blue organic light-emitting diodes based on anthracene derivatives *J Mater Chem* **20** 1560-6

[128] Klimes J, Bowler D R and Michaelides A 2010 Chemical accuracy for the van der Waals density functional *J. Phys.-Condens. Mat.* **22** 022201

[129] Klimes J, Bowler D R and Michaelides A 2011 Van der Waals density functionals applied to solids *Phys. Rev. B* **83** 195131

[130] Lazic P, Atodiresei N, Caciuc V, Brako R, Gumhalter B and Bluegel S 2012 Rationale for switching to nonlocal functionals in density functional theory *J. Phys.-Condens. Mat.* **24**

[131] Jenkins S J 2009 Aromatic adsorption on metals via first-principles density functional theory *Proceedings of the Royal Society a-Mathematical Physical and Engineering Sciences* **465** 2949-76

[132] Sun D Z, Kim D H, Le D, Borck O, Berland K, Kim K, Lu W H, Zhu Y M, Luo M M, Wyrick J, Cheng Z H, Einstein T L, Rahman T S, Hyldgaard P and Bartels L 2010 Effective elastic properties of a van der Waals molecular monolayer at a metal surface *Phys. Rev. B* **82** 201410

[133] Mortensen J J, Hansen L B and Jacobsen K W 2005 Real-space grid implementation of the projector augmented wave method *Phys. Rev. B* **71** 035109

[134] *e.g. in VASP, setting LORBIT=12 yields the desired quantities.*

[135] Cheng Z H, Chu E S, Sun D Z, Kim D, Zhu Y M, Luo M M, Pawin G, Wong K L, Kwon K Y, Carp R, Marsella M and Bartels L 2010 Tunability in Polyatomic Molecule Diffusion through Tunneling versus Pacing *J. Am. Chem. Soc.* **132** 13578-81

[136] *According to the computer named Deep Thought as described in The Hitchhiker's Guide to the Galaxy.*

[137] Stowasser R and Hoffmann R 1999 What do the Kohn-Sham orbitals and eigenvalues mean? *J. Am. Chem. Soc.* **121** 3414-20

[138] Feibelman P J, Hammer B, Norskov J K, Wagner F, Scheffler M, Stumpf R, Watwe R and Dumesic J 2001 The CO/Pt(111) puzzle *J. Phys. Chem. B* **105** 4018-25

Appendix A

Appendix to Chapter 2: Introduction to Scanning Tunneling Microscopy (STM): interpretation and simulation of STM images

Here I present a derivation along the lines of the work in [15], with some simplifications and modifications where I think appropriate. The central idea is that we can model the effect of the STM tip on electron flow as being a sink (source) into (out of) which probability current flows so that over some finite region (R_{tip}) in the vicinity of the tip, electronic wave-vectors are not stationary states but instead are either losing or gaining electron density at a steady rate. Throughout the rest of the sample however, electron density remains constant because those electrons transferred to (or from) the tip are replenished (or lost) to the underlying reservoir that is the Cu substrate. If this is the case, then the sample/tip system can be modeled as:

$$\hat{H}|\varphi_E\rangle = E|\varphi_E\rangle + |\sigma\rangle, \qquad \text{(EQ A1)}$$

where $|\varphi_E\rangle$ is a steady-state wave-vector with energy E at locations where $|\sigma\rangle$ is 0, and has time dependence elsewhere. Later it will be necessary to re-express $|\varphi_E\rangle$ in terms of true steady-state wave-vectors (i.e. those that would exist if no current were flowing through the tip) as these wave-vectors (call them $|\varepsilon_i\rangle$) can be calculated with DFT whereas the original $|\varphi_E\rangle$ cannot. The wave-vector $|\sigma\rangle$ encapsulates the effective current-sink/source properties of the tip (the details of which generally are not known due to experimental limitations), where based on the model described above:

$$\langle \vec{r}|\sigma\rangle = \begin{cases} \sigma(\vec{r}\,), & if\ \vec{r} \in R_{tip} \\ 0, & otherwise. \end{cases} \qquad \text{(EQ A2)}$$

The function $\sigma(\vec{r})$ on the right hand side of equation A2 indicates a non-zero valued function that because we don't know its details must otherwise be left generic. The probability current due to the $|\varphi_E\rangle$ (whose "steady-state" energy is *E*) flowing into or out of any position $\vec{r}$ in space is simply given by the time dependence of the observable density $\rho_E(\vec{r})$ whose associated operator is $\hat{\rho}_{\vec{r}} = |\vec{r}\rangle\langle\vec{r}|$ which can be found by taking its commutator with the Hamiltonian:

$$\begin{aligned} \partial_t \rho_E(\vec{r}) &= \partial_t \langle \varphi_E|\hat{\rho}_{\vec{r}}|\varphi_E\rangle \\ &= \frac{1}{i\hbar}\langle \varphi_E|\,[\hat{\rho}_{\vec{r}}\,, \hat{H}]\,|\varphi_E\rangle \\ &= \frac{2}{\hbar}\Im\langle \varphi_E|\,\hat{\rho}_{\vec{r}}\,\hat{H}\,|\varphi_E\rangle. \end{aligned}$$

In the final step I used the fact that a complex number minus its conjugate is just twice the imaginary part multiplied by i. The component of measured current due to the state $|\varphi_E\rangle$ (call it I_E) should therefore be given by integrating $\partial_t \rho_E(\vec{r}\,)$ over all of space (though notably it will be non-zero only in the region R_{tip}), yielding

$$\begin{aligned} -I_E &= \frac{2}{\hbar}\Im\langle \varphi_E|\hat{H}|\varphi_E\rangle \\ &= \frac{2}{\hbar}\Im\langle \varphi_E|(E|\varphi_E\rangle + |\sigma\rangle) \\ &= \frac{2}{\hbar}\Im\langle \varphi_E|\sigma\rangle, \end{aligned} \qquad \text{(EQ A3)}$$

where equation A1 has been substituted for $\hat{H}|\varphi_E\rangle$ and the fact that $\Im\langle\varphi_E|\varphi_E\rangle = 0$ has been used. The negative sign in front of I_E is due to the convention that current should measure the flow of positive charge.

As noted in chapter 2, the only electrons contributing to the current should be those lying between the Fermi energies of the sample and tip so that the total measured current is

$$I = \frac{2}{\hbar} \int_{E_F}^{E_F+eV} dE \ \Im\langle\varphi_E|\sigma\rangle. \qquad \text{(EQ A4)}$$

Here the minus sign for current has disappeared because when V is negative, as is the case for negative current flow (i.e. electrons hopping into the tip), the limits of integration shown above will flip to yield an overall negative sign and therefore negative current. To solve for $|\varphi_E\rangle$ in terms of the states that can be calculated ($|\varepsilon\rangle$), equation A1 can be rearranged and a complete set of states inserted:

$$\begin{aligned} |\sigma\rangle &= \left(\hat{H} - E\right) \int_{-\infty}^{\infty} d\varepsilon \ |\varepsilon\rangle\langle\varepsilon|\varphi_E\rangle \\ &= \int_{-\infty}^{\infty} d\varepsilon \ (\varepsilon - E)|\varepsilon\rangle\langle\varepsilon|\varphi_E\rangle. \end{aligned} \qquad \text{(EQ A5)}$$

This suggests inversion of the operator $\left(\hat{H} - E\right)$ to solve for $|\varphi_E\rangle$ in terms of $|\sigma\rangle$. As can be seen from equation A5 however, such an inversion will contain a singularity for those states that have eigenvalues $\varepsilon = E$. One option would be to reserve ourselves to solutions $|\varphi_E\rangle$ that have no contributions from such states, however in doing so we would find that these solutions have no imaginary part when substituted into the equation for measured current, equation A4. Furthermore, if a contribution to $|\varphi_E\rangle$ from the $|\varepsilon = E\rangle$ states is incorporated (by adding an arbitrary linear combination of them) it will still be found that there is no current in equation A4 because a quick insertion of an $\langle\varepsilon = E|$ state on the left of equation A5 shows that $|\sigma\rangle$ has no projection onto $\langle\varepsilon = E|$. That is, the original formulation of the problem (equation A1) leads to contradiction if one wishes to measure current by calculating $\partial_t \rho_E(\vec{r})$ associated with the number of electrons either "disappearing" or "appearing" at the tip.

The problem here is that we are trying to model something using the mathematical machinery of quantum mechanics that requires breaking (or at least bending) the rules enforced by that mathematical machinery. Specifically, we have a system that is allowing particles to appear or disappear into some closed region (R_{tip}) contained within the system's bounds – the advantage of trying to solve the problem this way is that we no longer need to model the entire macro-scale electronics of the STM that allow current to flow out of the tip and be measured. The standard tweak that is used to get around this problem is to couple the states $|\varphi_E\rangle$ to some imaginary wave-vector space by modifying the original Hamiltonian to include a small imaginary potential:

$$\hat{H} \rightarrow \hat{H} + i\delta,$$

where, in order to preserve the original physics of the problem, we will require that $\delta \rightarrow 0$ in some limit. The problem of solving for $|\varphi_E\rangle$ can now be reformulated as:

$$\begin{aligned} |\varphi_E\rangle &= (\hat{H} - E + i\delta)^{-1}|\sigma\rangle \\ &= \int_{-\infty}^{\infty} d\varepsilon \frac{|\varepsilon\rangle\langle\varepsilon|}{\varepsilon - E + i\delta} |\sigma\rangle \\ &= \left(\mathcal{P} \int_{-\infty}^{\infty} d\varepsilon \frac{|\varepsilon\rangle\langle\varepsilon|}{\varepsilon - E} - i\pi \ \mathrm{sgn}(\delta) \int_{-\infty}^{\infty} d\varepsilon \, |\varepsilon\rangle \, \delta(\varepsilon - E)\langle\varepsilon| \right) |\sigma\rangle. \end{aligned}$$

The final line follows from complex contour integration, with the letter $\mathcal{P}$ indicating that the first integral is to be taken as a principle value (it incorporates only those values of ε on the real line that do not include the singularity at $\varepsilon = E$). Substituting this expression back into equation A4 yields the current measured by the STM. In doing so, the first term above disappears as it has no imaginary part, and we are left with:

$$I \propto \int_{E_F}^{E_F+eV} dE \;\; |\langle \varepsilon | \sigma \rangle|^2. \qquad \text{(EQ A6)}$$

If additionally it is assumed that $\sigma(\vec{r})$ is a delta function centered at the location of the tip (i.e. $|\sigma\rangle \propto |\vec{r}_{tip}\rangle$), then equation A6 is further simplified to read:

$$I \propto \int_{E_F}^{E_F+eV} dE \;\; \rho_E(\vec{r}_{tip}),$$

as claimed in equation 2.2 of Chapter 2. In the ideal case of a point-like tip this is perfectly reasonable. As discussed in Chapter 2, non-ideal tips can often be modeled by sampling $\rho_E(\vec{r})$ in some phenomenological way.

Appendix B

Appendix to Chapter 4: AQ Network Models

Figure B.1 shows an excerpt from the table of pores that can be constructed based on how neighboring AQ molecules bond to one another on the Cu (111) surface.

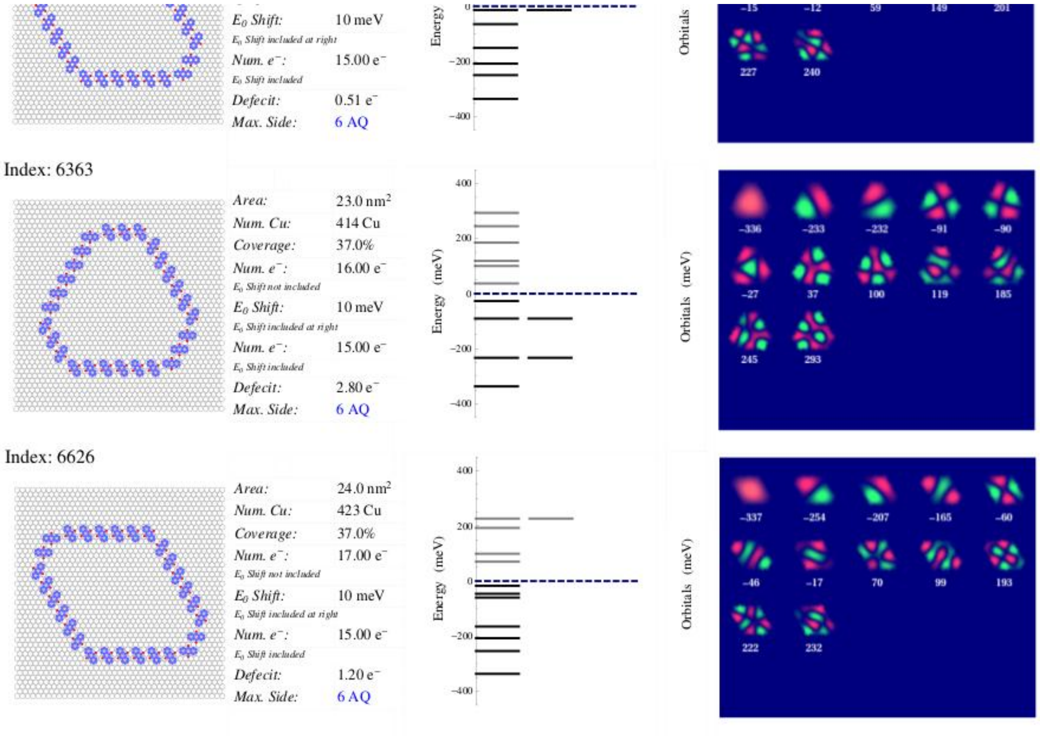
E_0 Shift: 10 meV
E_0 Shift included at right
Num. e^-: 15.00 e^-
E_0 Shift included
Defecit: 0.51 e^-
Max. Side: 6 AQ

Index: 6363

Area: 23.0 nm^2
Num. Cu: 414 Cu
Coverage: 37.0%
Num. e^-: 16.00 e^-
E_0 Shift not included
E_0 Shift: 10 meV
E_0 Shift included at right
Num. e^-: 15.00 e^-
E_0 Shift included
Defecit: 2.80 e^-
Max. Side: 6 AQ

Index: 6626

Area: 24.0 nm^2
Num. Cu: 423 Cu
Coverage: 37.0%
Num. e^-: 17.00 e^-
E_0 Shift not included
E_0 Shift: 10 meV
E_0 Shift included at right
Num. e^-: 15.00 e^-
E_0 Shift included
Defecit: 1.20 e^-
Max. Side: 6 AQ

Figure B.1 Library of geometrically possible AQ network pores.